

Near-IR Spectra of Red Supergiants and Giants

I. Models with Solar and with Mixing-Induced Surface Abundance Ratios ^{*}

A. Lançon¹, P.H. Hauschildt², D. Ladjal^{1,3}, and M. Mouhcine⁴

¹ Observatoire Astronomique de Strasbourg, Université L. Pasteur & CNRS (UMR 7550), Strasbourg, France

² Hamburger Sternwarte, Gojenbergsweg 112, 21029 Hamburg, Germany

³ Institute of Astronomy, Katholieke Universiteit, Celestijnenlaan 200 B, 3001 Leuven, Belgium

⁴ Astrophysics Research Institute, Liverpool John Moores University, Twelve Quays House, Egerton Wharf, Birkenhead, CH41 1LD, UK

Received July 2006 / Accepted 2 January 2007

ABSTRACT

Context. It remains difficult to interpret the near-IR emission of young stellar populations. One main reason is our incomplete understanding of the spectra of luminous red stars.

Aims. This work provides a grid of theoretical spectra of red giant and supergiant stars, that extends through optical and near-IR wavelengths. For the first time, models are also provided with modified surface abundances of C, N and O, as a step towards accounting for the changes that occur due to convective dredge-up in red supergiants or may occur at earlier evolutionary stages in the case of rotation. The aims are (i) to assess how well current models reproduce observed spectra, in particular in the near-IR, (ii) to quantify the effects of the abundance changes on the spectra, and (iii) to determine how these changes affect estimates of fundamental stellar parameters.

Methods. Spectra are computed with the model atmosphere code PHOENIX and compared with a homogeneous set of observations. Although the empirical spectra have a resolution of only $\lambda/\Delta\lambda \sim 1000$, we emphasize that models must be calculated at high spectral resolution in order to reproduce the shapes of line blends and molecular bands.

Results. Giant star spectra of class III can be fitted extremely well at solar metallicity down to ~ 3400 K, where difficulties appear in the modelling of near-IR H₂O and TiO absorption bands. Luminous giants of class II can be fitted well too, with modified surface abundances preferred in a minority of cases, possibly indicating mixing in excess of standard first dredge-up. Supergiant stars show a larger variety of near-IR spectra, and good fits are currently obtained for about one third of the observations only. Modified surface abundances help reproducing strong CN bands, but do not suffice to resolve the difficulties. The effect of the abundance changes on the estimated T_{eff} depends on the wavelength range of observation and can amount several 100 K.

Conclusions. While theoretical spectra for giant stars are becoming very satisfactory, red supergiants require further work. The model grid must be extended, in particular to larger micro-turbulent velocities. Some observed spectra may call for models with even lower gravities than explored here (and therefore probably stellar winds), and/or with more extreme abundances than predicted by standard non-rotating evolution models. Non-static atmospheres models should also be envisaged.

Key words. Stars: fundamental parameters – Stars: red supergiants – Stars: red giants – Stars: atmospheres – Stars: spectra

1. Introduction

Red supergiants and red giants are the most luminous stars in, respectively, star forming or old passive galaxies. Being cool, they are the dominant sources of near-IR light. In highly reddened starburst galaxies, the near-IR

light from red supergiants is sometimes the only direct information available on the stellar populations. Models for their spectra are thus important, even though they are also particularly difficult to construct (rich molecular line spectrum, extended atmospheres). If they are successful in reproducing empirical spectra, it will be legitimate to use them instead of observed spectral libraries in future analyses of galaxies.

Recently, Levesque et al. (2005) have shown that up-to-date models compare well with optical observations of red supergiants, and shown that this success helps in explaining the location of observed red supergiants

Send offprint requests to: A. Lançon e-mail: lancon@astro.u-strasbg.fr

^{*} Selected theoretical spectra (see text) can be retrieved in FITS format at CDS via anonymous ftp to cdsarc.u-strasbg.fr (130.79.128.5), or via <http://cdsweb.u-strasbg.fr/cgi-bin/qcat?J/A+A/>

in the HR-diagram. At near-IR wavelengths (1–2.5 μm), the most prominent molecular features are those of CO and CN. Their sensitivity to surface gravity and effective temperature (T_{eff}) has been the basis of the 8-colour classification system of White & Wing (1978), although they are also sensitive to other parameters (Tsuji 1976, McWilliam & Lambert 1984, McGregor 1987, Bessell et al. 1991, Origlia et al. 1997). Strong CN bands are predicted for low gravity stars with temperatures around 4500 K, and are indeed observed in local red supergiants (Lançon & Wood 2000) and in extragalactic objects such as the bright star clusters of M 82 (Lançon et al. 2003). However, it had not been verified until now whether models are capable of reproducing the strengths of various CN and CO bands throughout the near-IR range simultaneously. Nor whether they can match optical and near-IR properties together.

An important aspect not accounted for in recent collections of model spectra for red supergiants is internal mixing. Standard stellar evolution predicts non-solar surface abundance ratios due to convective dredge-up in the red supergiant phase (Iben 1966, Maeder 1981). Early observations had pointed out the inadequacy of solar abundance ratios in individual cases (e.g. α Ori, Beer et al. 1972). More recently, both theory and observations showed that main sequence rotation or other processes are capable of mixing CNO-cycle products into the atmosphere even before the red supergiant phase is reached (Maeder & Meynet 2001, Trundle & Lennon 2005). In red supergiants, He and ^{14}N surface abundances are typically enhanced while ^{16}O and ^{12}C abundances are reduced. Modified abundances of C,N and O alter the relative strengths of the predominant molecules.

In this paper, we present recent PHOENIX models specifically computed to address some of the above points. The emphasis is on the effects of non-solar abundance ratios of C,N and O; a more complete study of other parameters (in particular micro-turbulent velocities) has been started and will be reported in a forthcoming paper. The model assumptions are described in Sect. 2 and the predicted colours and molecular features in Sect. 3. In Sect. 4 and 5, the models are compared with spectroscopic data covering wavelengths from 1 to 2.4 μm or, for a subsample, from 0.51 to 2.4 μm . Giants of class III, luminous giants of class II and supergiants of class I are discussed successively. The discussion in Sect. 6 focuses on fundamental parameter determinations from spectra, including the effects of mass and surface abundances on T_{eff} . A brief conclusion summarizes the results.

2. PHOENIX models with solar and modified abundances

2.1. Summary of model ingredients

The model atmospheres and synthetic spectra were computed with PHOENIX version 13.11.00B. The model setup is identical to that of Kučinskas et al. (2005). We recall

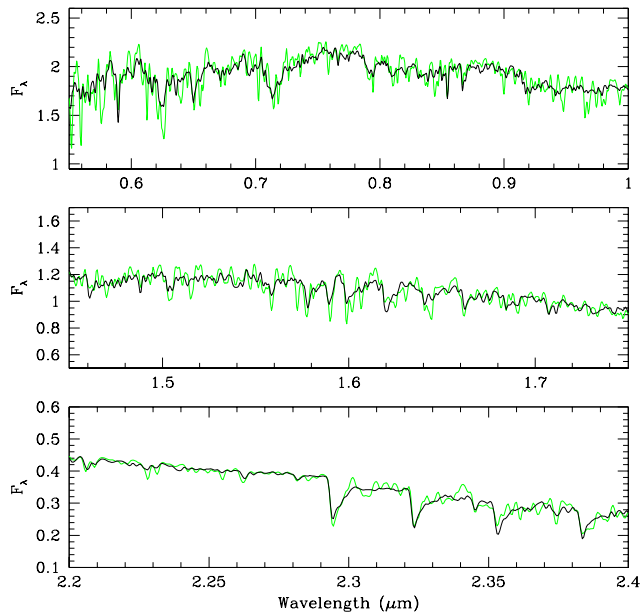


Fig. 1. Typical differences between PHOENIX spectra obtained with an initial wavelength sampling step of 2 \AA (grey) and 0.1 \AA (black). Both spectra have been smoothed by convolution with a gaussian with FWHM=15 \AA . The models shown have $T_{\text{eff}}=4000$ K, $\log(g)=1$, $M=1 M_{\odot}$, but differences are important for any of the calculated models. Only the high resolution calculations match the data.

only the most relevant details here. The models are computed in spherical symmetry. A mixing length to pressure scale height ratio of 2.0 is used for all models. Dust is allowed to form in the atmospheres but is assumed to immediately rain out of the photospheric layers; therefore, no dust opacities are used in the models shown here. This is an important assumption for cool models with large extensions. In addition, all models presented here have large enough gravities to not produce a radiatively driven wind and, therefore, winds are not included.

The model spectra were computed specifically for comparison with data that has a spectral resolving power of order 1000, i.e. $\Delta\lambda \simeq 10 \text{\AA}$ at 1 μm . *Nevertheless, we emphasize that the model spectra must be computed at high spectral resolution before smoothing, in order to sample individual absorption line profiles properly and to obtain low resolution spectra that resemble observations* (Fig. 1). We used a wavelength sampling step of 0.1 \AA throughout. Using only half these points produces negligible changes at $\lambda > 8000 \text{\AA}$ (0.1 % rms), and small variations in the shapes of the strongest optical bands at $\lambda < 8000 \text{\AA}$ (2 % rms). The small sampling step used here is an important change with respect to previous collections of PHOENIX spectra, which were computed with an initial wavelength sampling step of 2 \AA (e.g. Kučinskas et al., 2005, and models included in the library of Martins et al., 2005).

The models discussed cover effective temperatures ranging from 2900 to 5900 K and gravities in the set $\log(g)=\{-1,-0.5,0,1,2\}$ (cm.s^{-2}). The micro-turbulent velocity is set to a constant value of $v_{\text{mic}}=2\text{ km s}^{-1}$, except in a few exploratory models. Values of 2 to 3 km s^{-1} are typical for red giant stars (Smith & Lambert 1985). A more extensive grid of models covering higher values of this parameter is in the process of being calculated. Two stellar masses are considered: $1M_{\odot}$ and $15M_{\odot}$. Models at $9M_{\odot}$ were also computed, but the differences with the $15M_{\odot}$ ones are negligible. For $M=1M_{\odot}$, many of the calculations at $\log(g)=-1$ did not converge (radiation pressure incompatible with the assumption of no winds), and this mass-gravity combination is therefore excluded from the discussion. We also restrict the discussion to optical and near-IR wavelengths, with a focus on wavelengths between 0.81 and $2.4\mu\text{m}$.

2.2. Abundances

The reference set of models assumes solar abundances, based on the review of Grevesse & Noels (1993). The values most relevant to our study are summarized in Col. 2 of Tab. 1. A subset of models with solar-scaled abundances but $\log(Z/Z_{\odot})=-0.3$ was also computed but will only be discussed briefly in Sect. 6.2.

The second set of models has the same metallicity $Z=0.02$ as the reference set, but modified abundances of ${}^4\text{He}$, ${}^{12}\text{C}$, ${}^{14}\text{N}$, ${}^{16}\text{O}$ (Col. 5 of Tab. 1). In the following, the adopted modified abundances will be referred to as “RSG-specific abundances”.

The RSG-specific abundances were selected by inspection of the evolutionary tracks of Schaller et al. (1992; their case of standard mass loss) for stars with initial masses above $7M_{\odot}$, at evolutionary timesteps with effective temperatures below 4500 K. The values selected are representative of the final red supergiant stages of a star of initial mass $20M_{\odot}$ ($T_{\text{eff}}\simeq 3550\text{ K}$). Stars of lower initial masses would have RSG abundances closer to the main sequence values, while the tracks at $25M_{\odot}$ reach significantly larger modifications (tracks above $25M_{\odot}$ don’t extend to the low effective temperatures of red supergiants). Note that the initial mass fractions of Schaller et al. (1992) are not exactly the same as assumed in our reference set (mainly because of their larger He abundance), but that these differences are small compared to those that distinguish red supergiants from zero age main sequence stars.

In Tab. 1, the adopted abundances are compared to other values in the literature. The tracks of Meynet et al. (1994) assume larger mass loss rates than those of Schaller et al. (1992). More ingredients distinguish the models of Bressan et al. (1993) from those of the Geneva group. Nevertheless, predicted surface abundance alterations are of a comparable amplitude. Evolutionary tracks for stars with initial rotation predict that comparable ${}^{14}\text{N}$ enhancements are reached already by the end of the main sequence (Meynet & Maeder 2000, 2003), and are further increased

during the RSG phase. The achieved abundance ratios depend strongly on initial rotation velocity, on initial mass and on mass loss prescriptions. One major difference between rotating and non-rotating models is the length of time a star spends as a red supergiant with modified abundances in one and the other case (see also Maeder & Meynet 2001).

Mixing also occurs along the red giant branch and asymptotic giant branch for low and intermediate mass stars. The RSG-specific abundances adopted here are more extreme than those obtained through 1st dredge-up on the RGB (e.g. Iben 1964, Charbonnel et al. 1996, Girardi et al. 2000). In particular, the RSG-specific enrichment in He and ${}^{14}\text{N}$ and the drop in H and ${}^{12}\text{C}$ are larger than expected from 1st dredge-up. More mixing may however occur through second dredge-up on the early asymptotic giant branch (for stars with initial masses above about $4M_{\odot}$, e.g. Becker & Iben 1979, Boothroyd & Sackmann 1999), and though “non-standard” extra mixing for low mass stars that have evolved on the red giant branch past the RGB-bump (Charbonnel 1994, Charbonnel & do Nascimento 1998). Both these processes affect relatively luminous giant stars. The second one seems to be less efficient at the quasi-solar metallicities we consider than for population II stars. Therefore, we expect our RSG-specific abundances *not* to be appropriate for most solar neighbourhood giants of class III, while they might be relevant to some giants of class II.

We note that future calculations with modified surface abundances will include mixing-induced enhancements in the ${}^{13}\text{C}$ abundance, since ${}^{13}\text{CO}$ is a clear feature in near-IR spectra of cool stars. The effects of recent changes in measurements of the solar abundance ratios (Asplund et al. 2005) will also be investigated.

2.3. Spectra in numerical form

The model spectra for $M=1M_{\odot}$ with solar abundances, for $M=15M_{\odot}$ with solar abundances, and for $M=15M_{\odot}$ with RSG-specific abundances, are made available in FITS format through CDS. Because the quality assessments made in this paper are restricted to resolutions of order 10^3 in the near-IR (and a few hundred at wavelengths below $0.81\mu\text{m}$), the spectra made available are smoothed with a Gaussian to a full width at half maximum of 2 \AA . The initial models, calculated with a wavelength step of 0.1 \AA , can be requested from A.L. or P.H.H.

3. Trends in the models

Spectra illustrating the effects of mass, gravity and surface abundances are provided in Fig. 2. In this section, we will discuss quantitative trends using selected colours and molecular band indices. The indices are measured for each spectrum using: (i) the standard J, H, K filter passbands of Bessell & Brett (1988); (ii) narrow and intermediate-band filters as described in Tab. 2. All narrow and intermediate filter passbands are approximated with rectangles

Table 1. Surface abundances (by mass)

Element (1)	Adopted reference set (2)	Geneva 1992-1994 ZAMS (3)	Padova 1993 ZAMS (4)	Adopted RSG-specific set (5)	Geneva 1994 RSG (6)	Padova 1993 RSG (7)
¹ H	0.703	0.680	0.700	0.580	0.55	0.63
⁴ He	0.280	0.300	0.280	0.400	0.43	0.35
¹² C	0.0030	0.0044	0.0049	0.0022	0.0020	0.0032
¹⁴ N	0.00092	0.0014	0.0012	0.0065	0.0080	0.0051
¹⁶ O	0.0083	0.0106	0.0106	0.0076	0.0068	0.0084

Notes: **Col. 2:** Abundances adopted in our reference set of solar metallicity models. **Col. 3:** For comparison, main sequence abundances of Schaller et al. (1992), also used by Meynet et al. (1994). Metal abundance ratios based on Anders & Grevesse (1989). **Col. 4:** Main sequence abundances of Bressan et al. (1993). Metal abundance ratios based on Grevesse (1991). **Col. 5:** Abundances adopted in our RSG-specific set of models (see text). **Col. 6:** Final RSG abundances of Meynet et al. (1994) for 20 M_{\odot} stars. **Col. 7:** Final RSG abundances of Bressan et al. (1993) for 20 M_{\odot} stars.

Table 2. Filter and index definitions

Filter	Center (μm)	Width (\AA)	Notes
104	1.0395	50	quasi-continuum (1)
108	1.0800	60	CN (1)
110	1.1000	50	quasi-continuum near CN (1)
220	2.2000	1100	quasi-continuum (2)
236	2.3600	800	1st overtone CO (2)
COH	1.6222	80	2nd overtone CO
COHc1	1.6160	30	absorption-minimum near CO
COHc2	1.6285	30	absorption-minimum near CO
Index	Definition (3)		
I04-220	$-2.5 \log(104/220) + \text{cst}$		
CO(2.3)	$-2.5 \log(236/220) + \text{cst}$		
CO(1.6)	$-2.5 \log[2 \text{COH}/(\text{COHc1} + \text{COHc2})] + \text{cst}$		
CN(1.1)	$-2.5 \log(110/108) + \text{cst}$		

Notes : (1) Adapted from the 8-colour system of R.F. Wing (White & Wing 1978). (2) Adapted from Frogel et al. (1978). (3) cst stands for a constant that gives the index the value 0 for a model spectrum of Vega.

of identical central wavelength and width as the filters in the original references (as already done by Bessell et al. 1989). A model Vega spectrum provides the zero points in all passbands.

3.1. Colours

As shown in Fig. 3, colours that combine flux measurements around $1.04 \mu\text{m}$, in the J band and in the K band are good indicators of T_{eff} in theory, as their sensitivity to surface gravity is low. Above 3400 K, the spread in $\log(g)$ corresponds to a full spread in T_{eff} of about 200 K for the $15 M_{\odot}$ models (left panel). For $1 M_{\odot}$ models, the corresponding spread is much smaller: about 60 K, centered on a line very close to the models at $15 M_{\odot}$ and $\log(g)=0$. At the lowest temperatures, contamination of the pseudo-continuum in the K band with H_2O absorption leads to reduced fluxes in low gravity stars. Unfortunately, in the two-colour plots useful for observers the extinction vectors run almost exactly parallel to the temperature sequence

(right panel): more resolved spectral information is necessary to estimate an effective temperature from near-IR data.

Figure 4 illustrates the gravity dependence of colours involving H band fluxes. At high gravities, the minimum of the opacity of H^- around $1.6 \mu\text{m}$ produces a distinct hump in the H band spectra, with correspondingly blue H-K and red J-H colours. At low gravities, molecular absorption due mainly to CO and CN erases this continuum opacity feature. Such an effect was already mentioned by Bessell et al. (1991), though their interpretation probably underestimated the rôle of CN as compared to CO. The observations of Lançon et al. (2007) and those described in Kućinskas et al. (2005) provide a convincing validation of the JHK colours of the new models.

The effect of mass on the H band flux is insignificant at $\log(g)>0$. For lower gravities, H-K increases by up to only 0.02 magnitudes when going from 15 to $1 M_{\odot}$, at $T_{\text{eff}}>4000$ K.

Switching from solar-scaled to RSG-specific abundances has the following (small) effects on the above colours. All colours tend to become bluer. Colour differences in H-K and J-H remain smaller than 0.04 mag (and are <0.02 mag for most stellar parameters). The colour index 104–220 (defined in Tab. 2) is reduced by up to 0.08 mag. The bolometric corrections to the K band, BC(K), are essentially unchanged (the PHOENIX values agree with those of Levesque et al. 2005 to within a few percent between 3400 and 4300 K). Effects this small would be difficult to exploit on real stellar spectra.

3.2. Molecular indices

3.2.1. CO

CO is a long known indicator of luminosity class (Baldwin et al. 1973). It is sensitive to gravity and effective temperature, but also to metallicity and micro-turbulence. As indicated previously, a constant micro-turbulent velocity of 2 km.s^{-1} is used in this paper except in a few models. Large micro-turbulent velocities deepen the 1st overtone

PHOENIX models (v13), 3300 K and 4000 K

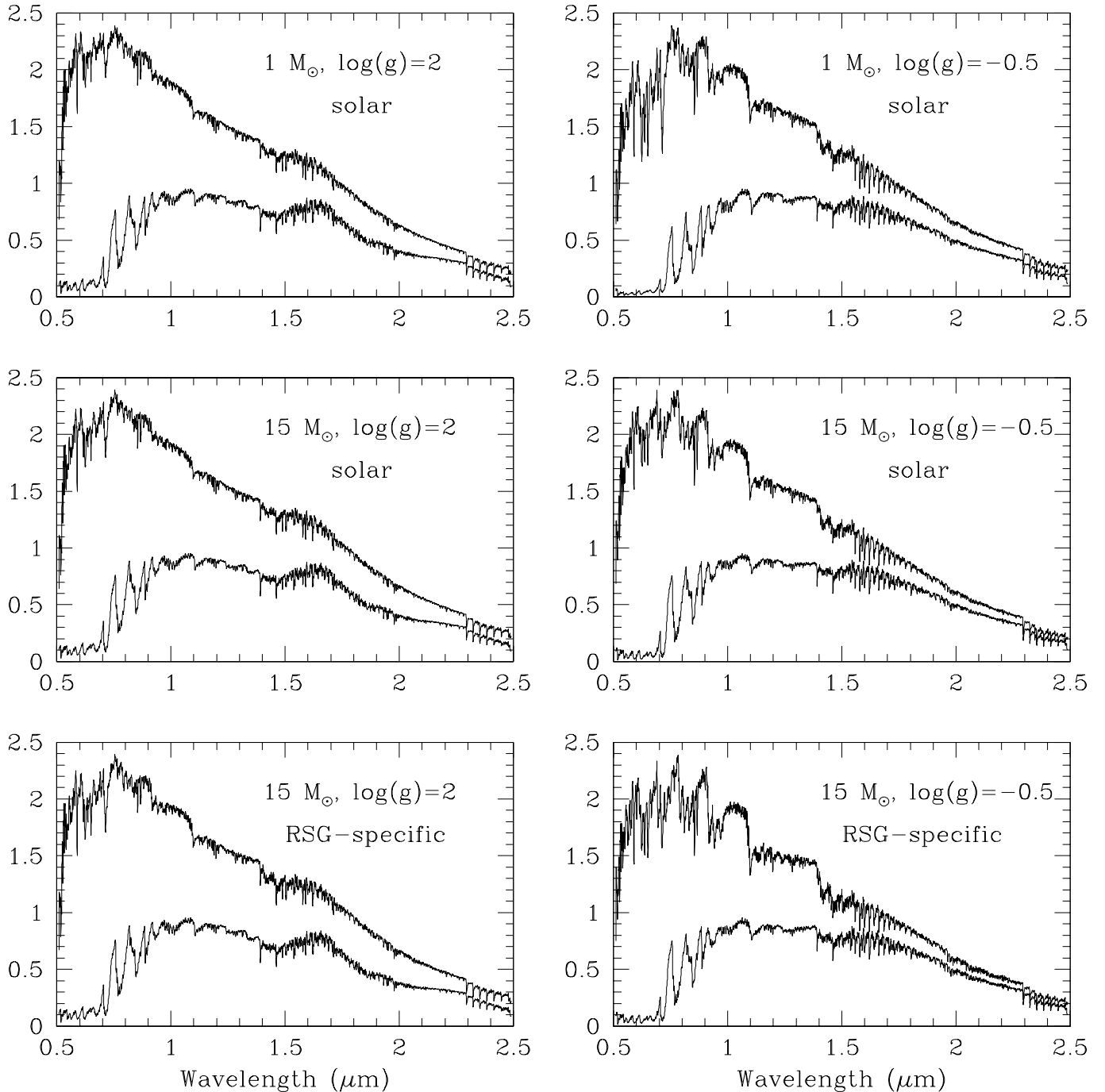


Fig. 2. Effects of gravity, temperature and surface abundances on PHOENIX model spectra. In each figure, the upper spectrum has $T_{\text{eff}} = 4000\text{ K}$ and the lower one $T_{\text{eff}} = 3300\text{ K}$. For easier comparison, fluxes have been normalized to values comparable to those in the upper left diagram. The figures on the left are at $\log(g)=2$, those on the right at $\log(g)=-0.5$. The upper figures are for solar abundances, the lower ones for RSG-specific abundances. The effect of mass ($1 M_{\odot}$ vs. $15 M_{\odot}$) is too small to be easily identified on this type of figure.

band of CO more than the 2nd overtone band, because line saturation is more important in the former than in the latter (e.g. Origlia et al. 1993, 1997 and refs. therein).

On the left panel of Fig. 5, the changes of the 1st overtone CO band at $2.29\ \mu\text{m}$ with gravity, temperature and

surface abundances are shown. As commonly found, CO increases with decreasing temperatures and gravities. The CO strength progressively levels off when $\log(g)$ takes negative values (i.e. the further dependence on g is negligible). Contamination by H_2O at high $\log(g)$ produces a drop of

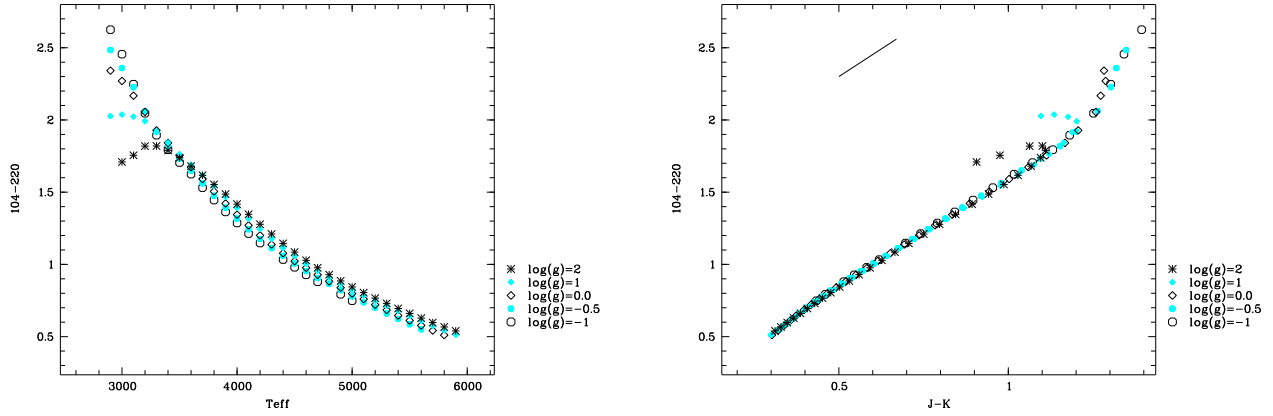


Fig. 3. Temperature sensitive near-IR colours (solar abundances, $15 M_{\odot}$). In the right panel, the effect of extinction on cool stellar spectra is shown for $A_V=1$ (using the extinction law of Cardelli et al. 1989, with $R_V=3.1$).

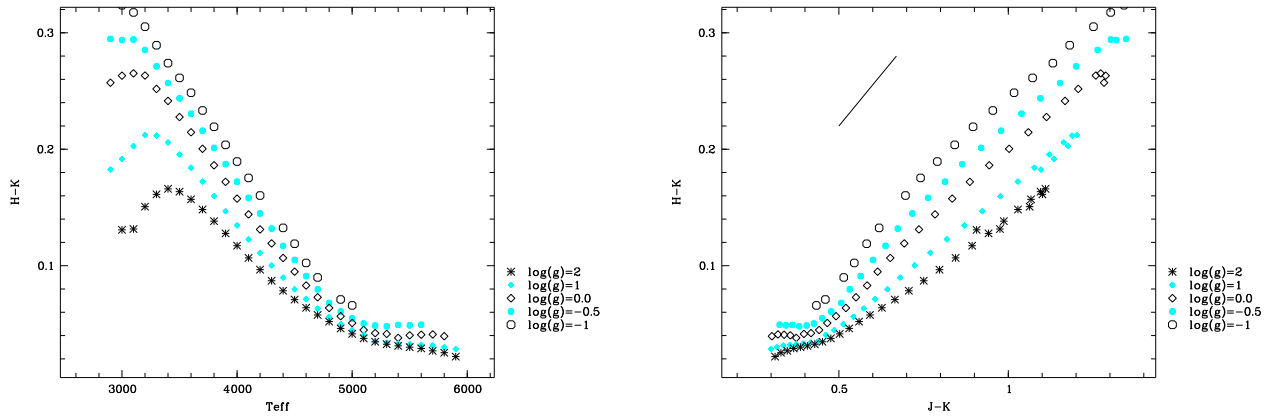


Fig. 4. Gravity sensitivity of $H-K$ (solar abundances, $15 M_{\odot}$). Extinction vector as in Fig. 3.

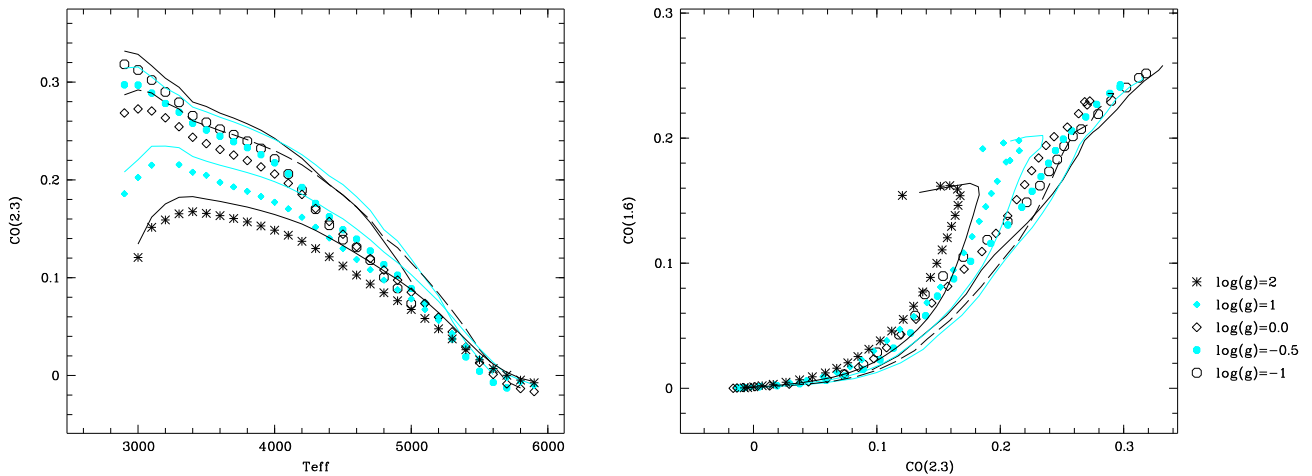


Fig. 5. Measurements of the strength of the 1st overtone CO band at $2.29 \mu\text{m}$ and of the 2nd overtone CO band at $1.62 \mu\text{m}$ in the model spectra ($15 M_{\odot}$). Symbols: temperature sequences at the indicated gravities, for RSG-specific abundances. Lines: corresponding sequences for solar-scaled abundances (black and light-coloured lines alternate, and the dashed line has $\log(g)=0$). Note that at a given $\text{CO}(2.3)$, $\text{xCO}(1.6)$ tends to be weaker in low gravity stars.

the CO index below 3200 K. Switching from solar to RSG-specific abundances reduces the CO strength generally by small amounts. The effect is maximum around 4500 K in low gravity models: RSG-specific models with $\log(g)=-1$ at 4500 K have the same CO index as solar abundance models with $\log(g)=2$, or alternatively with $\log(g)=-1$ but 4800 K.

The effects of $\log(g)$, T_{eff} and abundances on the apparent strength of the 2nd overtone CO band at $1.62 \mu\text{m}$ are similar, with two notable exceptions. First, the effects of changes in the abundance ratios are smaller than at $2.29 \mu\text{m}$. Second, low gravity saturation is reached earlier. The result is summarized in the right panel of Fig. 5. In particular, *low gravity stars tend to have weaker CO bands around $1.6 \mu\text{m}$ than high gravity ones, at a given strength of the $2.29 \mu\text{m}$ band.* Contamination of the H-band fluxes by CN absorption contributes to producing this trend, as already hinted at by Wing & Spinrad 1970.

Moving down from $15 M_{\odot}$ to $1 M_{\odot}$ has a negligible effect on the near-IR CO bands for $\log(g)>0$. At lower gravities, the $1 M_{\odot}$ CO bands are weaker than the $15 M_{\odot}$ bands (the effect is stronger for the $2.3 \mu\text{m}$ band than for the $1.6 \mu\text{m}$ bands).

3.2.2. CN

CN displays prominent near-IR absorption bands that have been studied extensively in the context of carbon star models (e.g. Loidl et al. 2001). The CN bands are prominent in red supergiants as well (White & Wing, 1978). While in carbon stars essentially all surface oxygen is locked into CO, CN coexists with other oxides in the atmospheres of red supergiants.

The behaviour of CN bands with varying model parameters is complex, as shown in Fig. 6. Bessell et al. (1989) describe the decrease of the CN $1.1 \mu\text{m}$ band strength with decreasing effective temperature below 3800 K, as well as its gravity dependence (stronger CN for lower gravities). Our more extended temperature range shows that the maximum CN strength is reached between 4200 and 4800 K. Both the location of the maximum and its actual strength depend on surface gravity, and on the chemical composition of the atmosphere. *CN bands are strongly enhanced in models with RSG-specific abundance ratios.* The effect of mass is small. CN is also enhanced when larger micro-turbulent velocities are assumed (Tsujii 1976). In empirical samples, spectra with strong CN absorption bands compared to their CO bands are candidates for modified surface abundances.

3.2.3. Other molecular bands longwards of $1 \mu\text{m}$.

H₂O. H₂O appears very abruptly in the models below a gravity-dependent threshold temperature: 3600 K at $\log(g)=1$, 3100 K at $\log(g)=-1$ (based on measurements in the K-band wings of the H₂O band centered near $1.9 \mu\text{m}$). Below this threshold T_{eff} , higher gravi-

ties lead to stronger spectral bands. Varying the mass between 1 and $15 M_{\odot}$, or switching to RSG-specific abundances, has only small effects on the H₂O bands. **TiO.** Near-IR TiO bands around $1 \mu\text{m}$ (TiO δ , $\Delta\nu = -1$) and $1.25 \mu\text{m}$ (TiO ϕ , $\Delta\nu = -1$) appear progressively in the models below a gravity-dependent temperature: ~ 3600 K at $\log(g)=1$, ~ 3400 K at $\log(g)=-2$ (based on visual inspection of the spectra in that region). Other near-IR TiO bands longwards of $1 \mu\text{m}$, such as the ϕ , $\Delta\nu = 0$ band near $1.12 \mu\text{m}$ are hidden in CN absorption. Again, varying the mass between 1 and $15 M_{\odot}$, or switching to RSG-specific abundances, has only small effects. We note that the next version of PHOENIX calculations will include an update of the TiO partition function and of the electron f -values of the TiO bands for the AMES TiO line list (Schwenke 1998), which appears to improve spectral synthesis results for M dwarfs (Allard et al., in preparation).

VO. The $1.05 \mu\text{m}$ VO band (VO A–X $\Delta\nu = 0$) is significant in the model spectra only at $T_{\text{eff}} \leq 3200$ K for $\log(g) \leq 1$. The effect of mass or abundances is small.

4. Models versus data in two-colour plots

In this and the following sections, we compare the models with the data collected by Lançon & Wood (2000) and Lançon et al. (2007). Both sets provide spectra at a spectral resolving power of order 1000 between $0.97 \mu\text{m}$ (sometimes $0.81 \mu\text{m}$) and $2.4 \mu\text{m}$. The first set adds low resolution extensions through the optical range down to 5100 \AA for a few of the stars. The merged sample contains luminous stars of spectral types G3I to M5I, G3II to M3II, and G5III to M5III, as well as asymptotic giant branch variables for comparison.

As shown in Fig. 7, the agreement between models and data is excellent in near-IR two-colour plots once extinction has been accounted for (see Sect. 5). Note that in this and the following figures the lines join models at constant $\log(g)$, while the data should follow real red giant or red supergiant branches. Evolutionary tracks predict that the warmer giants have $\log(g) \geq 2$ while the cool ones reach $\log(g) \simeq 0$. Red supergiants of various luminosity classes are expected to have $\log(g) \leq 0.5$.

Figure 8 combines measurements of the first and second overtone CO bands and the $1.1 \mu\text{m}$ CN band with J-K. Agreement between solar metallicity models and empirical data is good for *giant* stars. The strongest offset is noted for the second overtone CO bands in the H window, which tend to be too strong in the cool giant star models. The figures also suggest that modeled first overtone CO bands might be slightly too weak at low T_{eff} . Because extinction affects J-K, two-index diagrams with a negligible sensitivity to reddening are presented in Fig. 9. The same conclusions hold. The CO line list data are from Goorvitch & Chackerian (1994 a,b), and are known to work very well in the case of M dwarfs. Therefore, it is unlikely that the line list data for CO is the cause of the CO band discrepancies. We note that ^{13}CO contributes to the measured

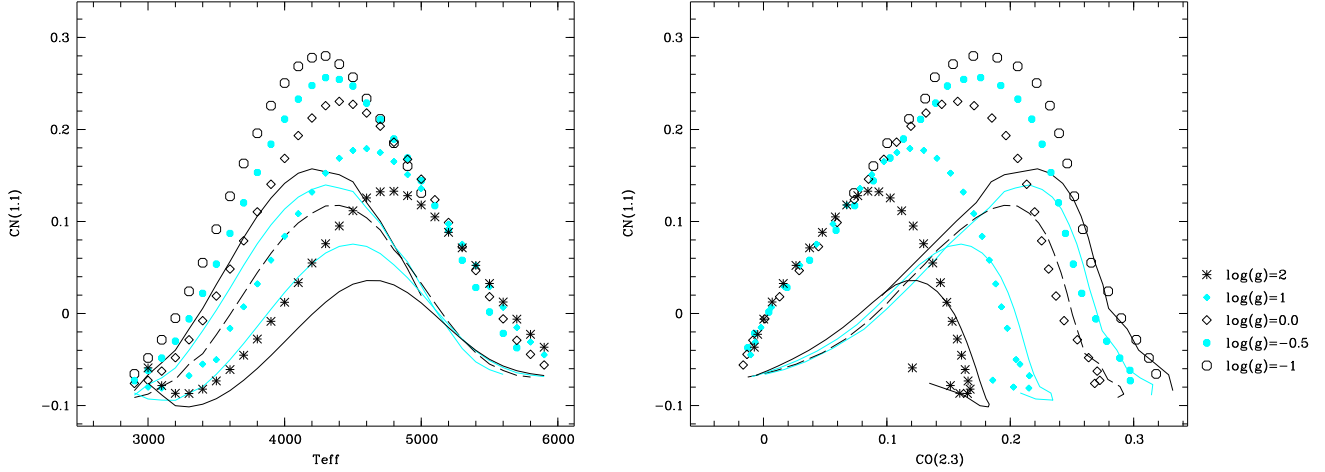


Fig. 6. Measurements of the strength of the CN band at $1.1 \mu\text{m}$ in the model spectra ($15 M_{\odot}$). Symbols and lines are as in Fig. 5. The main effect of a decrease of mass ($15 \rightarrow 1 M_{\odot}$) is a shift of the models at $\log(g) \leq 0$ to the left by up to 0.04 mag in the right hand panel.

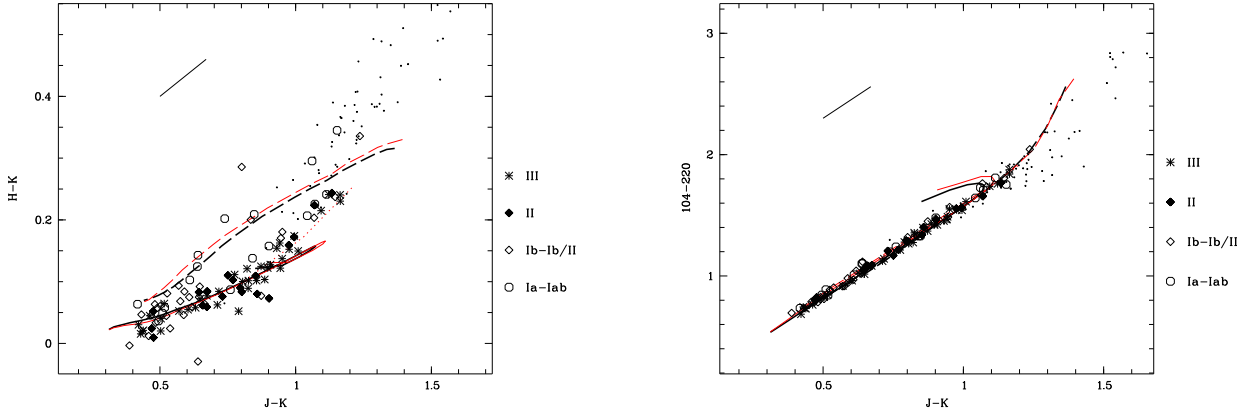


Fig. 7. Two-colour plots with observational and calculated data. The thin lines are T_{eff} sequences for solar abundances, the thick lines are for RSG-specific abundances. Solid lines are at $\log(g)=2$, dashed lines at $\log(g)=-1$. The dotted line follows models along an illustrative red giant branch at solar metallicity ($[T_{\text{eff}}(\text{K}), \log(g)] = [4200, 2], [3800, 1], [3400, 0]$). Symbols as explained are measurements on *dereddened* versions of the spectra of Lançon et al. 2007 (see Sect. 5), and dots O-rich Miras from Lançon & Wood 2000 (not dereddened). The reddening vectors are as in Fig. 3.

strength of the first overtone CO bands, and that changes in the ^{13}C abundances induced by stellar evolution may be responsible for some systematic effects. Slightly larger micro-turbulent velocities could improve the ratio of the first to the second overtone CO band strengths, but would also affect the CN bands. The outlier giant star near $J-K=0.7$ with weak band strengths is the only Population II star of the observed sample (HD 218732). Eye inspection of its spectrum reveals a metal poor atmosphere immediately. By contrast, the other giant stars appear to form a reasonably homogeneous sample in terms of metallicity.

While the trends with gravity present in the predicted molecular bands agree qualitatively with those observed, the molecular bands of only a fraction of the observed red *supergiants* can be reproduced quantitatively. Models with

RSG-specific abundances are favoured for a significant number of these objects, which show stronger CN bands than the solar metallicity models can produce. However, the CN and CO measurements show that despite the improvement achieved with the adopted changes in surface abundances, the model parameters explored here are not able to account for the whole range of molecular band strengths observed. Models with larger micro-turbulent velocities reach further into some of the areas occupied by real red supergiants, justifying the ongoing extension of the model grid. Alternatively, some red supergiants in nature may require even higher ^{14}N abundances than tested here or effective gravities lower than $\log(g)=-1$.

Comparisons between models and data on the star-by-star basis are provided in the following section.

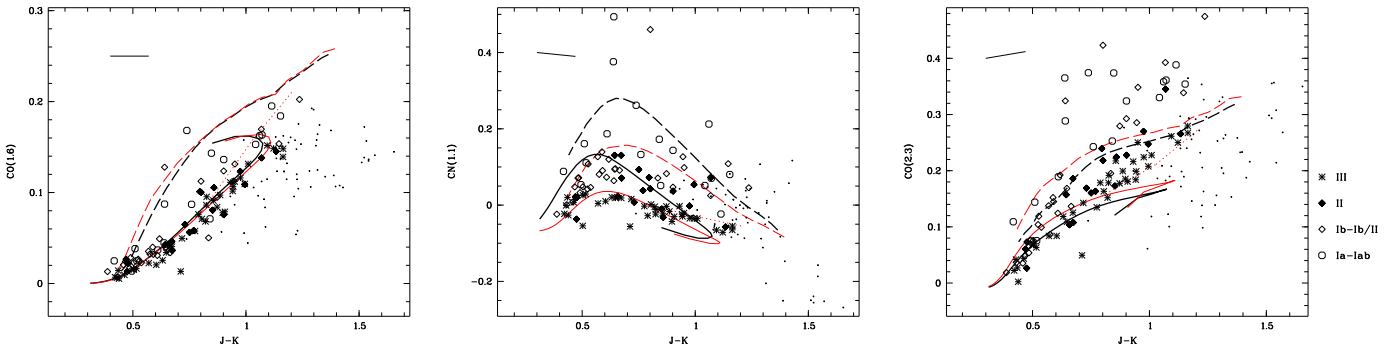


Fig. 8. Plots of molecular indices vs. colours with dereddened data. Symbols and lines are as in Fig. 7.

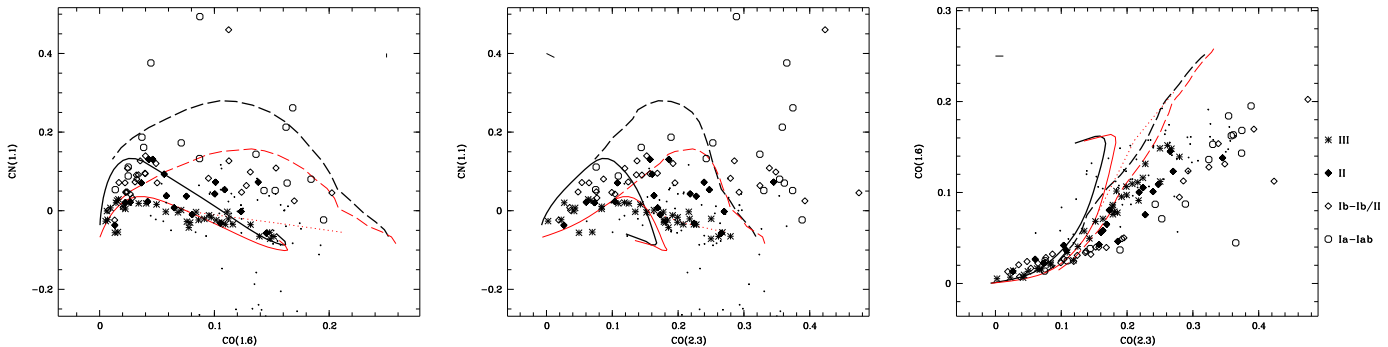


Fig. 9. Molecular index plots with dereddened data. Symbols and lines are as in Fig. 7.

5. Direct comparison between observed and theoretical spectra

5.1. Method

The comparison between models and data is based on the computation of reduced χ^2 differences. The theoretical spectra are smoothed to the resolution of the data, using gaussian broadening functions with adequate widths (note that for the optical spectra, whose resolution was seeing-dependent, we adopt a single smoothing value which in some cases underestimates the actual $\Delta\lambda$). They are then resampled to the wavelength step of the data, i.e. 5 \AA . A window function is used to eliminate the spectral intervals most strongly affected by telluric absorption, around 1.15 , 1.4 and $1.9\ \mu\text{m}$.

The rms noise of the data is modelled as being proportional to the square root of the signal. Numerical values given below assume an average signal-to-noise ratio of 50. This simple noise model is a reasonable representation of the typical high frequency noise of the data. The additional uncertainties due to flux calibration errors are not explicitly accounted for. They lead mainly to uncertainties in the estimated extinction values. A further discussion of the effects of the weighting of the data is provided in Sect. 6.1.

A mass of $1\ M_{\odot}$ is assumed for giants and bright giants, a mass of $15\ M_{\odot}$ for supergiants (see Sect. 6). For each empirical spectrum, the adopted algorithm loops through

all model temperatures and gravities (separately for the two sets of abundances). At each of these points, it also loops through an adequate set of extinctions (using the extinction law of Cardelli et al. 1989 with $R_V = 3.1$), and minimizes the χ^2 with respect to the extinction parameter A_V . The step in A_V is of $0.05\ \text{mag}$. A χ^2 map is produced in $T_{\text{eff}} - \log(g)$ space, and the 9 best fits (of the $T_{\text{eff}} - \log(g) - A_V$ space) are plotted for inspection. The χ^2 value of the 9th best fit is typically higher than for the 1st best fit by 10% when the best fits are good, and by only a few percent when they are poor. Typical uncertainties on the derived parameters in the case of *good* fits are $\pm 100\ \text{K}$ in T_{eff} , and ± 0.2 in A_V . For these good fits, gravity is usually determined to better than one step within our set of models ($\log(g) = -1, -0.5, 0, 1, 2$). Preliminary models with micro-turbulent velocities larger than $2\ \text{km s}^{-1}$ were tested only for supergiant star spectra and, in this paper, they are only discussed in cases where the initial fits were poor.

The method is robust with respect to errors in the positions of the individual molecular lines that jointly define the pseudo-continuum of the spectra at the resolution of interest here. Such errors were noted as a difficulty in the measurement of individual metal lines by Vanhollebeke et al. 2006. In order to verify this, we added random noise to the data at the level of a few percent, i.e. enough to completely alter the apparent positions of the blended CN

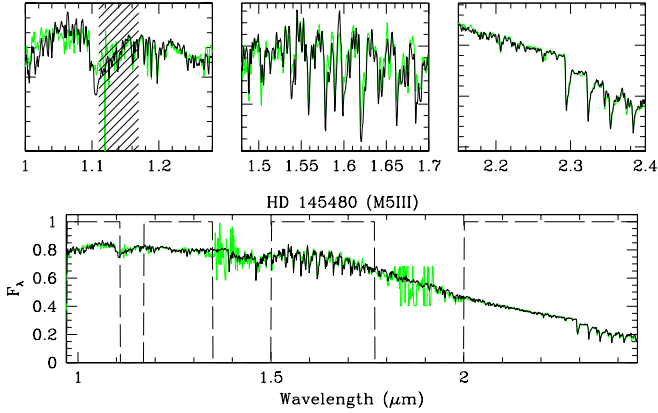


Fig. 10. Fit to a late type giant star spectrum (HD 145480, M5III). The data are shown as dotted lines, the model as a solid line. The window function for the χ^2 fit is also shown. Model parameters are 3400 K, $\log(g)=0$, $A_V=0.4$, $\chi^2 = 1.7$. Such a fit quality is typical for all the giants without available optical spectra.

lines between 2 and 2.3 μm . Differences in the derived parameters were well within the uncertainties stated above.

5.2. Giant stars

The data sample contains 35 stars of class III with spectral types G5 to M5 (after elimination of one particularly uncertain luminosity class and one known metal poor star with obviously weaker spectral features). Their shortest wavelength is 0.97 μm , except for 5 spectra with an optical extension.

Good fits are obtained for essentially all the near-IR spectra with the solar metallicity models. An example is given in Fig. 10. Among the satisfactory fits, there is a tendency for χ^2 to increase systematically from about 1 for types $\leq K4$ ($\chi^2=0.6-1.4$, depending on the actual S/N of individual spectra) to about 2 (1.5-2.5) for the M stars. This trend is due to a wealth of weak lines and deeper molecular bandheads at low temperatures, which among others induces a higher sensitivity of the value of the χ^2 to residual wavelength calibration errors or model line lists.

The χ^2 values for combined optical+near-IR spectra take values of 3 to 7 for satisfactory fits (considering the sensitivity of the χ^2 to the smoothing parameter at optical wavelengths and to flux calibration errors over such an extended wavelength range). Examples are shown in Fig. 11. The best fit to the spectrum of the coolest giant, the M5III star BS 4267 (= HD 94705) requires marginally negative extinction. Considering the flux calibration uncertainties and the choice of one particular extinction law, such a result is not alarming. Cooler models by only 100 K or models with higher $\log(g)$ by 0.5 would result in a positive value of the estimated A_V . The most obvious shortcoming of the models for giants this cool is an overprediction of the TiO absorption bands near 1 and 1.25 μm .

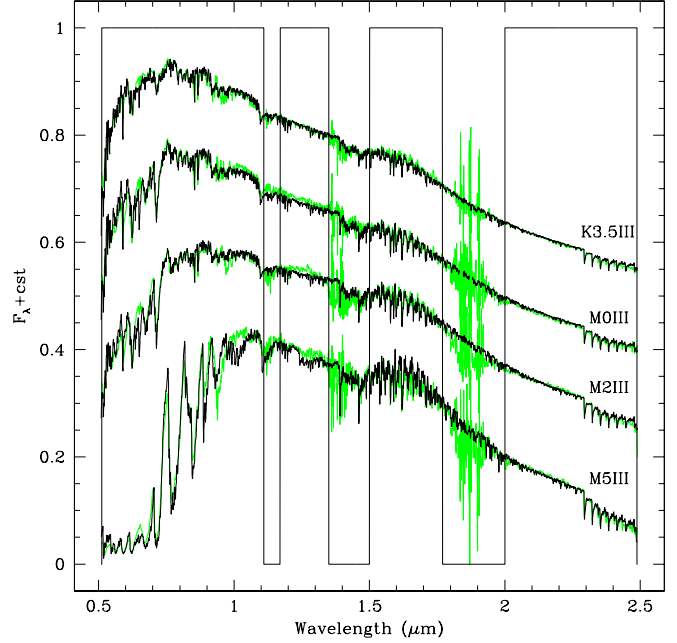


Fig. 11. Best fits to four giant star spectra that extend to optical wavelengths. Data are shown as dotted lines, best fit models as solid lines. The window function used to reject the noisiest spectral regions is also shown. From top to bottom: K3.5III star BS 4432 with model $[T_{\text{eff}}, \log(g), A_V, \chi^2] = [4100 \text{ K}, 2, 0.55 \text{ mag}, 2.3]$; M0III star BS 4371 with $[3900 \text{ K}, 1, 0.2 \text{ mag}, 4.5]$; M2III star BS 5301 with $[3800 \text{ K}, 1, 0.55 \text{ mag}, 5.2]$; M5III star BS 4267 with $[3300 \text{ K}, 1, -0.3 \text{ mag}, 13.9]$.

The results of the fitting procedure can be summarized as follows:

Temperatures range from 5300 K for type G5, to 3300 K for type M5. As expected from stellar evolution tracks, the highest available gravity ($\log(g)=2$) is selected for giants earlier than K7 (with one exception), then progressively more spectra are assigned $\log(g)=1$ and later 0. A_V values are spread between 0 and 1 (with 4 cases of marginally negative values). No correlation is found between A_V and T_{eff} .

Adopting the models with RSG-specific abundances rather than solar ones leads to poorer fits in all but one case. The values of the reduced χ^2 increase by 0.5 units on average. While the distribution of estimated effective temperatures for the sample is relatively flat with the assumption of solar abundances, it becomes bimodal with RSG-specific abundances: temperatures between 4500 and 5000 K are systematically avoided, because the CN bands of these models are too strong at the surface gravities of giant stars (cf. Fig. 6). This result was expected from Figs. 9 and 8. It is satisfactory as our set of RSG-specific abundances is not designed to match abundances in giant stars.

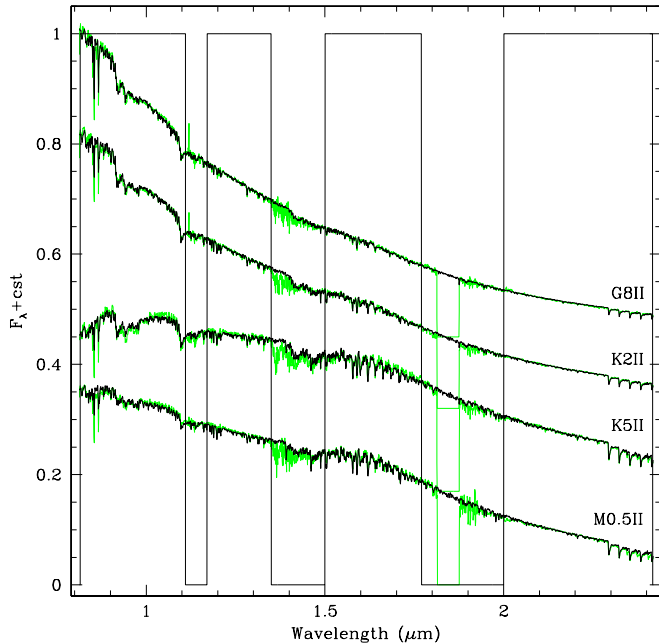


Fig. 12. Best fits to four bright giant star spectra (class II) that extend down to $0.81 \mu\text{m}$. Figure set-up is as in Fig. 11. From top to bottom: G8II star HD 150416 with $[T_{\text{eff}}, \log(g), A_V, \chi^2] = [5000 \text{ K}, 1, 0.1 \text{ mag}, 0.65]$; K2II star BD-29 2374 with $[4500 \text{ K}, 2, -0.15 \text{ mag}, 0.65]$; K5II star HD 168815 with $[4100 \text{ K}, 1, 1.3 \text{ mag}, 1.8]$; M0.5Ib star HD 132933 with $[4000 \text{ K}, 2, 0.4 \text{ mag}, 1.4]$. Among the above, we classify the K5II fit as satisfactory, the others as very good.

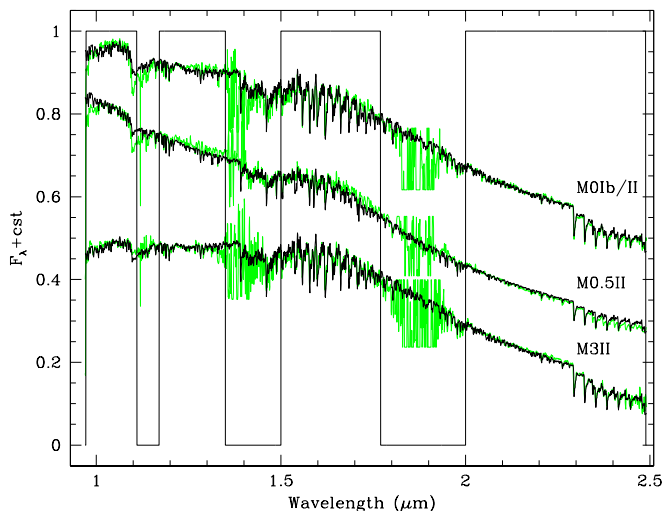


Fig. 13. Best fits to two bright giant star spectra for which the CN band at $1.1 \mu\text{m}$ is particularly poorly reproduced, and of the coolest class II star of the sample. Figure set-up is as in Fig. 11. From top to bottom: M0Ib/II star HD 145384 with $[T_{\text{eff}}, \log(g), A_V, \chi^2] = [3400 \text{ K}, -0.5, -0.15 \text{ mag}, 3.2]$; M0.5II star HD 142676 with $[3900 \text{ K}, 2, 0.0 \text{ mag}, 4.0]$; M3II star HD 153961 with $[3500 \text{ K}, 0, 1.0 \text{ mag}, 3.3]$.

5.3. Bright giants

The sample contains 29 bright giants of class Ib/II or II. Spectral types range from G3 to M3. None of the corresponding spectra extend through optical wavelengths, but 11 extend down to 8100 \AA . Their properties in terms of colours and molecular indices are spread between those of giants and supergiants. On average, they display slightly stronger bands of CO and significantly stronger bands of CN than giants of class III, at a given (dereddened) colour.

The solar metallicity model fits to all the spectra are satisfactory, two thirds of them being very good (Fig. 12). The models clearly contain all the molecular bands required. Marginally negative values of A_V are obtained in four cases, which is again not unexpected considering flux calibration uncertainties. The most common shortcomings found when the fits are not perfect are the following:

- There is a tendency for the models to show stronger CO bands at $2.29 \mu\text{m}$ and weaker CN bands at 0.93 and $1.1 \mu\text{m}$ than observed. This problem is only detectable clearly when the data extend down to $0.81 \mu\text{m}$.

- For stars with spectral types around K5II whose spectra extend down to $0.81 \mu\text{m}$, the models struggle to reproduce the energy distribution around $1 \mu\text{m}$, where it peaks between deep CN bands. This difficulty is certainly related to the strength of the CN bands at those temperatures (see Fig. 6).

- In two cases (spectral type M0Ib/II and M0.5II), the model CN bands are too weak while CO is reproduced well (Fig. 13).

The T_{eff} and $\log(g)$ scales obtained for the bright giants have a scatter similar to those found for giants and supergiants and are located between the two, as expected. Bright giants with spectral types earlier than K4 (included) are assigned $\log(g)=2$ (with one exception: HD 170457, G8Ib/II), and values of $\log(g)$ for types K5-M3 are scattered between 1 and -0.5 . No correlation is found between A_V and T_{eff} .

When moving from solar abundances to RSG-specific abundances, the χ^2 test indicates that the fits are degraded in a majority of cases (typically by $0.5 \chi^2$ units, as for the sample of class III stars). However, a significantly improved χ^2 is obtained for 4 stars, and the χ^2 changes are insignificant in 7 cases.

The improvements correspond to four stars of type K2 to M0 (out of the 11 bright giants available in this range), with estimated T_{eff} of 4300 to 3400 K. Eye inspection of the corresponding four spectra shows that the decrease in χ^2 corresponds to a better fit to the CN bands, which were not deep enough (by small amounts) in the solar metallicity models. In some cases, the improved χ^2 was associated with a decrease in T_{eff} by 100 K or an increase of $\log(g)$ by one bin size, but statistics are too small to define significant trends.

Degraded fits are frequently associated with excessive strengths of the model CN bands when the RSG-specific abundances are used. The T_{eff} -distribution obtained with the RSG-specific abundances still shows a zone of avoid-

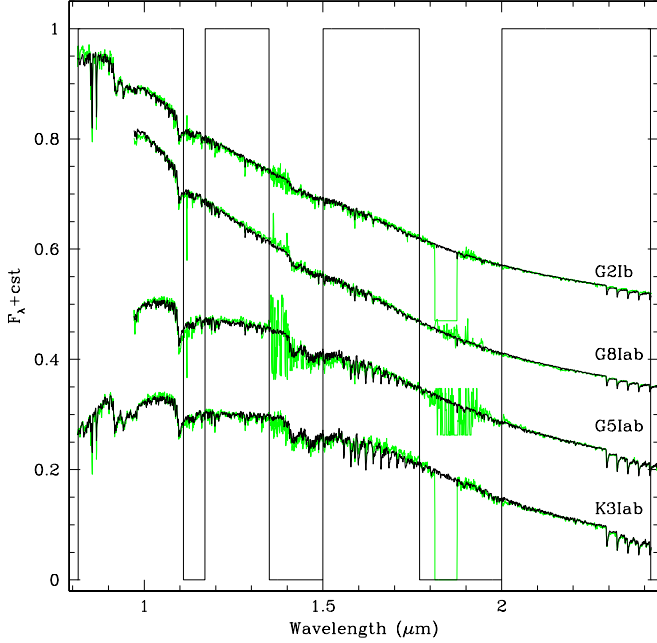


Fig. 14. Good and reasonable best-fits to warm red supergiant spectra (class I). Figure set-up is as in Fig. 11. Abundances are solar. From top to bottom: G2Ib star HD 182296 with $[T_{\text{eff}}, \log(g), A_V, \chi^2] = [5000 \text{ K}, 0, 0.95 \text{ mag}, 1.3]$; G8Iab star HD 206834 with $[4900 \text{ K}, 1, 0.3 \text{ mag}, 0.85]$; G5Iab star HD 170234 with $[4500 \text{ K}, 0, 2.15 \text{ mag}, 1.8]$; K3Iab star HD 187238 with $[4100 \text{ K}, 0, 1.65 \text{ mag}, 2.2]$. We have not counted the K3Iab case as a good fit, because the model CO bands around $1.7 \mu\text{m}$ are too strong. Note that the spectral type of the second and third stars are likely to be incorrect.

ance between 4500 and 5000 K, but the effect is not as obvious as in the case of class III stars. Although small number statistics affect this result, we note that all class II spectra with estimated T_{eff} in that range have poorer fits with the RSG-specific abundances than with solar ones. As expected, models with the adopted RSG-specific abundances do not apply to the majority of class II stars but they do allow us to identify candidate objects that may have suffered more than standard dredge-up.

5.4. Supergiant stars

The data sample contains 37 spectra of stars of class I, Ia, Iab or Ib (after removal of one particularly odd case that is probably misclassified and of one spectrum with poor correction for telluric absorption). Spectral types range from G2 to M5. The stars with the latest spectral types ($\geq \text{M2}$) are all known or suspected variables (as are the vast majority of late type supergiants in nature). 9 spectra, all with spectral type M, extend through the optical range; note that the optical and near-IR spectra of individual objects were taken within less than three weeks of each other. 8 spectra extend down to $0.81 \mu\text{m}$.

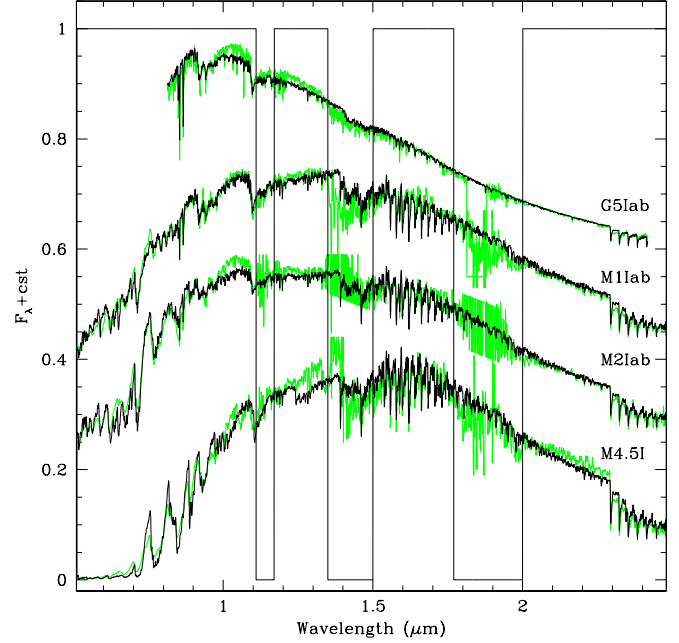


Fig. 15. A selection of marginally acceptable best-fits to red supergiant spectra. Figure set-up is as in Fig. 14. From top to bottom: G5Iab star HD 165782 with $[T_{\text{eff}}, \log(g), A_V, \chi^2] = [4900 \text{ K}, -1, 2.4 \text{ mag}, 2.8]$; M1Iab star HD 98817 with $[3700 \text{ K}, -1, 1.8 \text{ mag}, 7.8]$; M2Iab star BS 3364 (= HD 72268) with $[3500 \text{ K}, -0.5, 1.0 \text{ mag}, 12.4]$; M4.5I star V774 Sgr with $[3200 \text{ K}, -0.5, 1.7 \text{ mag}, 22.7]$.

Good fits to the red supergiant spectra with solar metallicity models are obtained for 13 of the 37 spectra, all of which are of spectral type G2-G8. 16 of the remaining spectra find a model representation that is still reasonable (though often significantly poorer than the fits we called satisfactory within class II above). These are spread over the whole range of spectral types and include some of the data that extend through optical wavelengths. In general, stars of luminosity class Ib are easier to fit than those of class I, Ia or Iab, and all class Ib stars of our sample can be matched well or reasonably well. Finally, we classify 7 of the red supergiant fits as poor. Five of these correspond to variable stars with spectral types later than M3.5 (class I, Ia or Iab), the two others are of spectral type M0Ia and G5Ia.

Figures 14, 15 and 16 illustrate some of the good, intermediate and poor model fits.

The main shortcomings of the models when the fits are of *intermediate* quality are the following :

- A relatively common feature is a shortage of flux in the models around $1 \mu\text{m}$, as seen in two spectra of Fig. 15. This problem was already mentioned for a few bright giants of class II, as a property that is associated with strong CN bands and can be identified only when the observed spectra extend far enough to short wavelengths.
- Even when the 1st overtone CO bands after $2.29 \mu\text{m}$ are reproduced reasonably well, it happens that the relative strengths of the 2nd overtone CO bands in the H

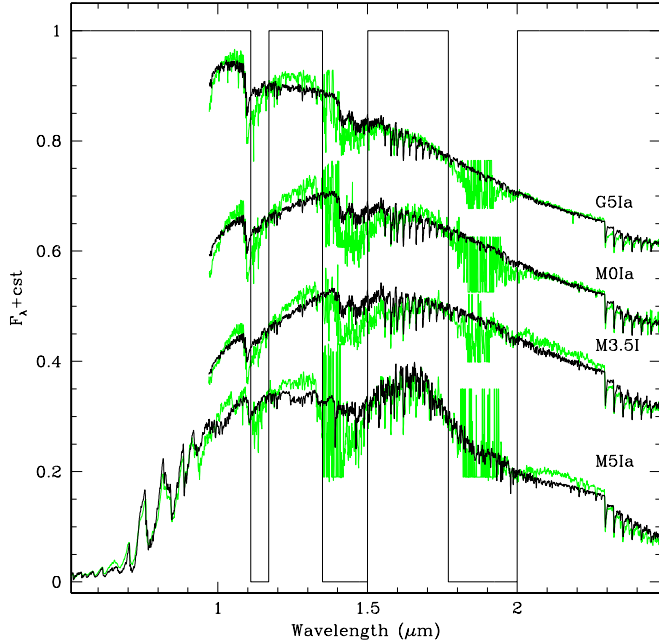


Fig. 16. A selection of poor best-fits to red supergiant spectra. Figure set-up is as in Fig. 14. From top to bottom: G5Ia star HD 155603 (classified K00-Ia by Keenan and McNeil, 1989) with $[T_{\text{eff}}, \log(g), A_V, \chi^2] = [4300 \text{ K}, -0.5, 1.8 \text{ mag}, 8.6]$; M0Ia star Trumpler 1-27 with $[4200 \text{ K}, -1, 4.4 \text{ mag}, 13.4]$; M3.5I star IRC -20427 with $[4000 \text{ K}, -1, 5.35 \text{ mag}, 15.2]$; M4-5Iab star CL Car with $[3300 \text{ K}, 2, 1.65 \text{ mag}, 21.6]$. The fits being of poor quality, the derived parameters are not reliable and are given here only for the sake of completeness.

window are incorrect, the transitions at longer H window wavelengths ($1.65\text{-}1.75 \mu\text{m}$) being too strong in the models compared to the data (last spectrum of Fig. 14 and 2nd and 3rd spectrum of Fig. 15).

— In the coolest models, bands of TiO appear (in particular near $1.25 \mu\text{m}$) that are not seen in the data.

Poor fits are obtained for the coolest stars (e.g. bottom spectrum of Fig. 16) and for stars with extreme CN bands (e.g. top three spectra of Fig. 16). We recall that the coolest stars are also variable and that discrepancies are to be expected in a comparison with static models. When the CN bands are strong, the derived temperatures are a compromise between the necessity to reproduce the energy distributions and the CO bands at $2.29 \mu\text{m}$ (which pulls towards low temperatures), and the need to maximize CN depths (which pulls towards 4100 K , cf. Fig. 6). When optical spectra are taken into account, the relative weight of the CN bands is reduced compared to CO, optical features and the energy distribution. On the contrary, when only wavelengths between 0.97 and $2.4 \mu\text{m}$ are available the rôle of the CN bands is large. This explains why in Fig. 16 such a large difference in T_{eff} is obtained between the M3.5Ia star (no optical spectrum, best fit $T_{\text{eff}} = 4000 \text{ K}$) and the M4-5I star (optical spectrum available, best fit $T_{\text{eff}} = 3300 \text{ K}$). The temperatures of the M0Ia and M3.5I

stars of that figure are most probably overestimated. For a similar reason, the temperature of the G5Ia star at the top of the figure may be underestimated (compare with the G5Iab star in Fig. 15).

A typical problem with the best fit models for the spectra with very strong CN is the relative strength of the various CO bands. The G5Ia star HD 155603 (Fig. 16) provides the most extreme example. It has the strongest $2.29 \mu\text{m}$ CO band of our whole supergiant sample and among the strongest CN bands as well, but in the H window CO is almost absent. None of the current models with $v_{\text{mic}} = 2 \text{ km s}^{-1}$ reproduces this combination. Models with larger micro-turbulent velocities improve the representation of these extreme spectra.

Water bands are another cause of disagreement between models and data. The near-IR bands of H_2O and CN overlap in wavelength to such a degree that confusion can occur (and has occurred in the past, cf. Wing & Spinrad 1970). The shapes of the $1.1 \mu\text{m}$ bands of H_2O and CN are subtly different (cf. Fig. 5 of Lançon & Wood 2000). The bands observed in red supergiants correspond closely to CN, although contamination with H_2O is possible. The H_2O band around $1.9 \mu\text{m}$, which is very deep and broad in Miras, is inconspicuous in red supergiants. It may be present at a low level in the coolest ones observed, such as CL Car (Fig. 16), which are semi-regular long period variables. The clearest H_2O signature in the observed red supergiant spectra is a sharp bandhead at $1.32 \mu\text{m}$, although the detection of this feature requires good corrections for telluric absorption bands. Based on this signature, the 7 coolest supergiants of our sample contain H_2O (all these are variable). The models however either do not show this bandhead (low g) or, when they do (high g), also display a $1.9 \mu\text{m}$ band that is much wider and deeper than observed.

Finally, the semi-regular variables V774 Sgr, EV Car and CL Car (Figs. 15 and 16) have a clear VO absorption band at $1.05 \mu\text{m}$ and small or inexistent absorption bands at $1 \mu\text{m}$ and $1.25 \mu\text{m}$, two properties that are not matched by the models.

When moving from the models with solar abundances to the RSG-specific abundances, the χ^2 test indicates that about a third of the fits are improved, another third are degraded, and the quality of the final third of the fits is essentially unchanged.

The deteriorations, when present, are not severe. In most cases, it seems that abundance values intermediate between the adopted solar and RSG-specific sets would provide optimal fits, which is not surprising considering that evolutionary tracks for red supergiants cover a range of abundances. Eye inspection shows that quite a few stars with equally good fits with both model sets also fall in this category.

The improvements obtained with RSG-specific abundances for a fraction of the red supergiants are significant, although they clearly do not resolve all the difficulties. They are associated with a better representation of

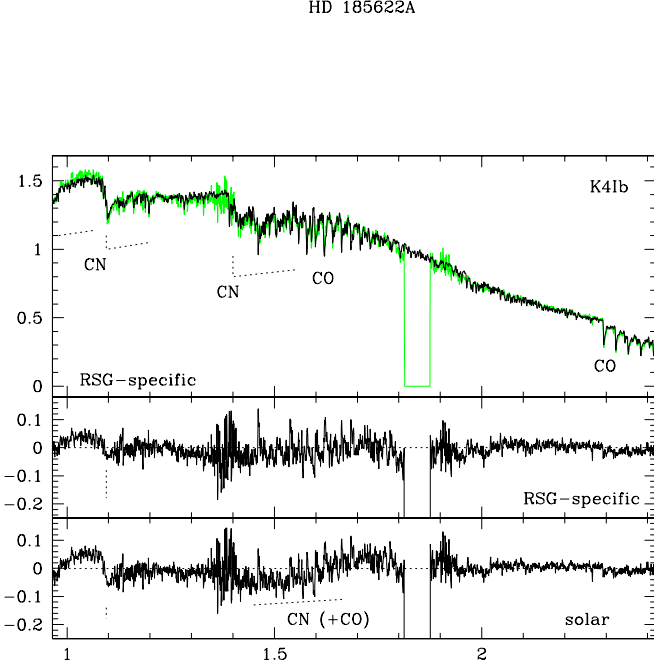


Fig. 17. *Top:* K4Ib star HD 185622a and best fit model with RSG-specific abundances. *Middle:* Residuals of the fit shown above (data–model). *Bottom:* Residuals of the best fit with solar metallicity models (χ^2 1.22 times larger than in the RSG-specific case). Note the CN residuals below $1 \mu\text{m}$, around $1.1 \mu\text{m}$ and in the slope between 1.45 and $1.75 \mu\text{m}$. These are typical and systematic shortcomings of the solar metallicity models in the cases where RSG-specific models provide a better fit.

the observed CN bands and sometimes also with a better match to the CO bands around $1.6 \mu\text{m}$ (see also Sect. 5.5). One may distinguish two subcategories of improvements. On one hand, some of the stars that already had reasonable model counterparts with solar abundances have better, often good adjustments with RSG-specific abundances. These are mainly stars of type G and K. An example is given in Fig. 17. On the other hand, the improvements refer to stars that had poor fits with solar abundances, and for which the RSG-specific abundances lead to somewhat better but still unacceptable fits. These are the same 7 stars as mentioned earlier. The models cannot simultaneously reproduce their CO bands (1.6 and $2.29 \mu\text{m}$), their CN bands and their energy distribution. More extended model grids are needed to characterize these objects. Problems related to H_2O , TiO and VO , when present, remain essentially unchanged.

The explored changes in surface abundances induce changes in the best-fit parameters for the sample of observed stars with maximal amplitudes of $\pm 200 \text{ K}$. For the sample as a whole, there is no strong correlation between the change in T_{eff} and the actual value of T_{eff} , which is not surprising considering that many fits are imperfect and that the behaviour expected from theory is complex (see Sect. 6.2).

The T_{eff} distribution of the red supergiant sample obtained under the assumption of RSG-specific abundances shows no anomaly. Scrutiny of the 2D distribution of estimated parameters in the $\log(g)$ – T_{eff} plane suggests that a narrow zone extending diagonally from $[\log(g)=0, T_{\text{eff}}=4000 \text{ K}]$ to $[\log(g)=1, T_{\text{eff}}=5000 \text{ K}]$ (with no extension to lower gravities) might nevertheless be underpopulated. The statistical significance of this gap is low because of small sample numbers. Its presence would favour a general picture in which RSG-specific abundances are only relevant to red supergiants with large initial masses or to late stages of red supergiant evolution.

5.5. Effects of the weighting of various parts of the spectra

Because there are *systematic* differences between the best fit models and the observed spectra, the best fit model parameters depend on the weights given to the various spectral features in the fitting procedure. Our standard method weights the data based on a reasonable simplified model for the high frequency noise in the data. This adopted weight is inversely proportional to the square root of the signal, i.e. spectral regions with large fluxes contribute more to the χ^2 than regions with small fluxes. Since the spectra of cool stars peak around $1 \mu\text{m}$ (in the flux density units adopted in this paper), molecular bands near this wavelength are important in the fit. In practice, this weighting makes CN bands relatively important and CO bands (around $1.6 \mu\text{m}$ and $2.3 \mu\text{m}$) comparatively unimportant.

If the noise was indeed gaussian, uncorrelated between pixels, and exactly of the amplitude assumed, then our procedure would select the models with the largest likelihoods. This is not the case (flux calibration errors, wavelength-dependent gains and contributions of the read-out noise, etc.), and therefore our weighting is in some ways non-optimal. We may choose various alternative methods (see Decin et al. 2004 for an interesting discussion of comparable issues). First, we may decide to fit measurements of the depths of one or several features rather than spectral segments. Unfortunately, the selection of one or the other feature remains somewhat arbitrary. Second, we may decide to focus on either the optical or the near-IR spectral range. This circumvents the difficulty of reproducing the global energy distribution (possible uncertainties in the relative flux calibration of the optical and near-IR data, uncertainties in the adopted extinction law, etc.). Third, we may keep the whole spectrum but explore the effects of alternative weightings. We briefly summarize below the main trends found while investigating these three options.

Figures 18 and 19 show how three important near-IR molecular features in the models compare with their observed counterparts, when our standard weighting procedure is applied to select the best fit. Note that the corresponding figures for H-K, J-H, J-K or 104-220 (not shown)

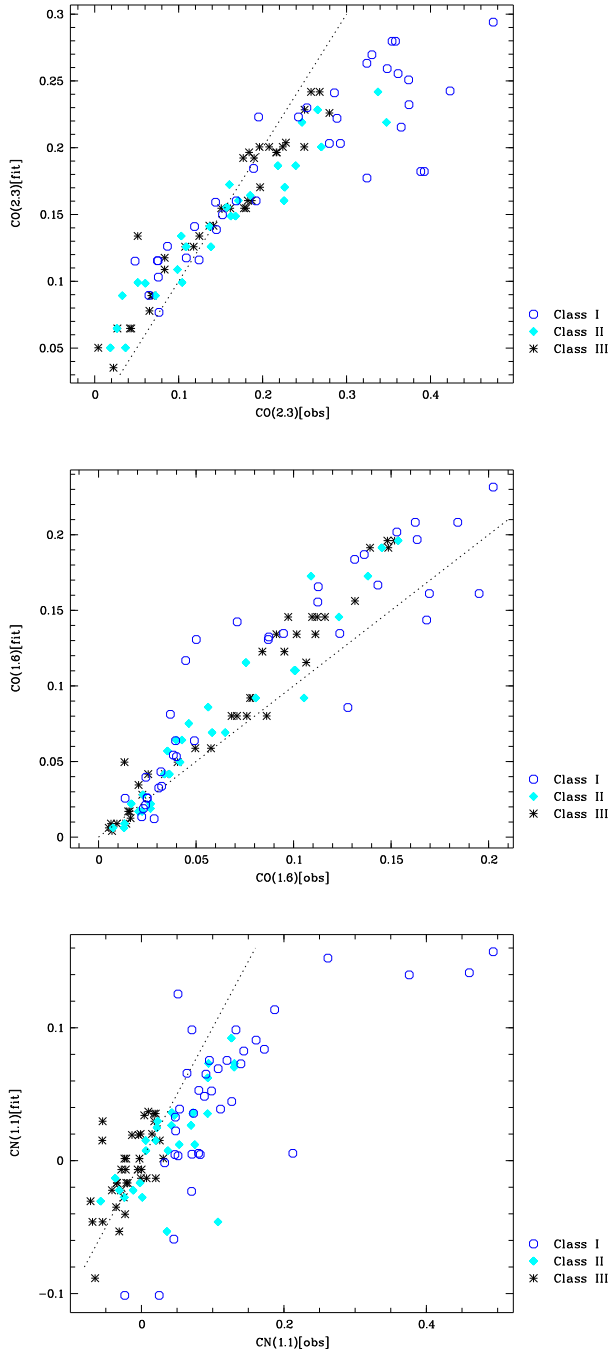


Fig. 18. *Top:* Strength of the $2.3\mu\text{m}$ CO band of the best fitting solar metallicity models versus strength of this band in the dereddened observed spectra (cf. Tab.2). The dotted line highlights the one-to-one relation. *Middle:* Same figure for the adopted measure of the $1.6\mu\text{m}$ CO band. *Bottom:* Same figure for the adopted measure of the $1.1\mu\text{m}$ CN band.

are very well behaved, which only states that the adopted extinction law is capable of dealing with the actual extinction (and with flux calibration errors) rather well.

As expected, systematic drifts away from the perfect match are smaller for the $1.6\mu\text{m}$ CO features than for the

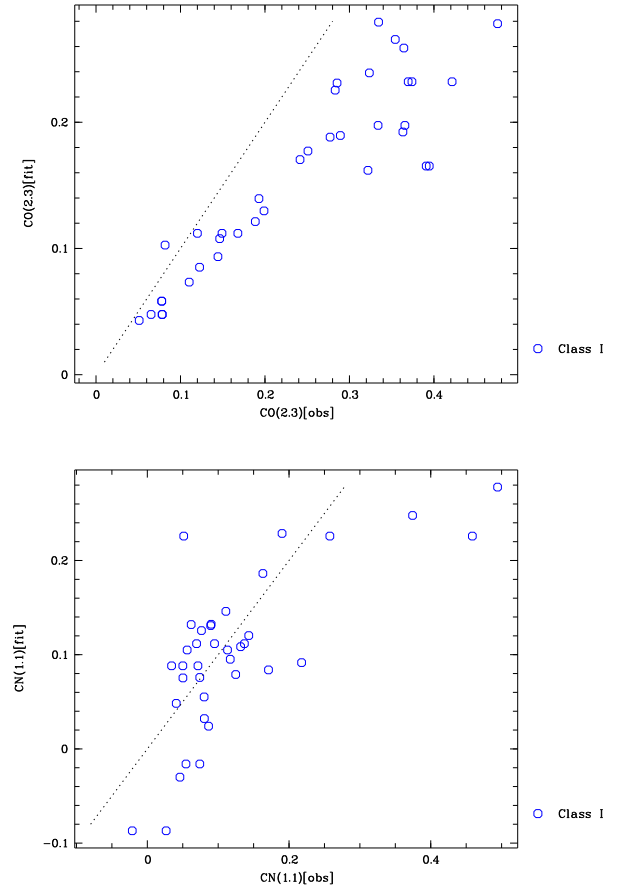


Fig. 19. Same as the top and bottom panels of Fig. 18 but for supergiants only, and using models with RSG-specific abundances.

$2.3\mu\text{m}$ CO band, the latter being located in a region of low flux (small contribution to the χ^2). The best-fit models have systematically deeper $2.3\mu\text{m}$ CO bands than the data for warm stars (types G and K), but systematically too shallow $2.3\mu\text{m}$ CO bands for the coolest stars (type M). By changing the weights in the fitting procedure (e.g. by assuming a constant signal-to-noise ratio), the $2.3\mu\text{m}$ bands can be reproduced better, but at the cost of a loss of the fit quality at shorter near-IR wavelengths.

The CN bands are reproduced well for giant stars. But they are too shallow in the best fit models for some of the bright giants and for the supergiants. Here, changing the fitting weights has a small effect compared to more fundamental model parameters such as abundances, gravities or micro-turbulence. RSG-specific abundances move the bulk of the red supergiants into a satisfactory location (Fig. 19). With RSG-specific abundances, the fits to CO bands around $1.6\mu\text{m}$ are not fundamentally improved or degraded on average, while the first overtone CO bands ($2.3\mu\text{m}$) of the best fits become shallower, i.e. too shallow. By assigning CO more weight in the fits, it is possible to reduce this discrepancy while still observing the global improvement for CN. But with the current grid of models,

no fully satisfactory solution can be found for any weighting scheme.

The weights given to various spectral ranges impact on the estimated stellar parameters. Examples have already been given in Sect. 5.4, and further discussions can be found below.

6. Discussion

Providing estimates of fundamental stellar parameters is a major application of theoretical spectra. Our discussion focuses on the determination of T_{eff} from near-IR spectra using the new PHOENIX models.

6.1. Stellar mass

We have mentioned in Sect. 3 that the effects of mass on colours and molecular indices, at a given T_{eff} and $\log(g)$, are small. The comparison between the best fit parameters obtained assuming $1 M_{\odot}$ and $15 M_{\odot}$ nevertheless reveals a trend worth highlighting : *for stars with high surface gravities ($\log(g)=2$), the temperatures obtained with $1 M_{\odot}$ models are systematically lower by ~ 100 K than those obtained with $15 M_{\odot}$ models.* This is particularly relevant to giants of class III, but also to the warmer of the bright giants of class II. Unfortunately, we found no systematic differences between the χ^2 values obtained with one or the other assumption on mass. Thus, *it is not currently possible to determine mass using spectral fits* such as those performed in this paper. Mass has to be fixed a priori by other means.

For luminous giants and supergiants, i.e. stars with low gravities, we found no systematic effect of mass on best-fit T_{eff} or $\log(g)$. The differences in T_{eff} between the two assumptions are scattered around 0 with typical values of ± 100 K (more in cases where even the best fits are not satisfactory). We note a correlation between the difference in T_{eff} and the difference in $\log(g)$: when a change in the assumed mass leads to a rise in the best-fit T_{eff} , it generally also produces a rise of the best-fit value of $\log(g)$.

6.2. T_{eff} -systematics related to surface abundances: model predictions

The effects of surface abundance ratios on T_{eff} estimates (and on derived gravities) are of larger amplitude than those of mass, and we therefore describe them in more detail. They can be studied by fitting a sample of solar metallicity models with models with RSG-specific abundances, using the procedure described for fits to observational data. *The results depend on the wavelength range adopted in the analysis.* They are illustrated in Fig. 20. The amplitude of the effect is of several hundred Kelvin. If we call δT_{eff} the difference between the input and output temperatures (output minus input), we find no simple linear correlation between δT_{eff} and T_{eff} .

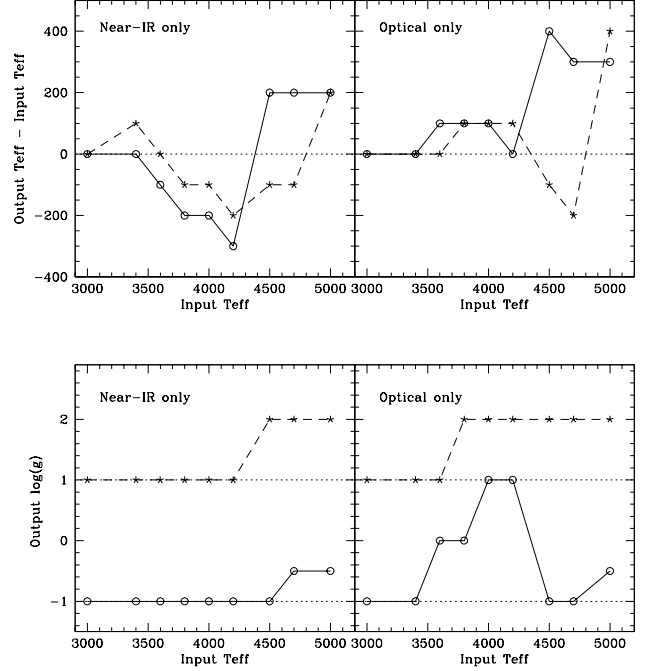


Fig. 20. Effects of the surface abundances on estimates of T_{eff} and $\log(g)$. The input T_{eff} and $\log(g)$ refer to solar metallicity models. The output parameters to the values obtained when fitting the solar metallicity spectra with models with RSG-specific abundances, using the procedure described in Sect. 5.1. *Solid:* Input $\log(g)=-1$. *Dashed:* Input $\log(g)=1$.

The figure based on near-IR data ($0.97\text{--}2.4 \mu\text{m}$, with the window and weight functions of Sect. 5.1) is tightly related to the behaviour of the near-IR CN bands. Output T_{eff} values around $4400\text{--}4900$ K (depending on gravity) are avoided because the CN bands of those RSG-specific models are too strong. A similar effect is present when optical wavelengths are used ($0.51\text{--}0.97 \mu\text{m}$), but it is combined in the low- T_{eff} range with a variety of effects due to oxides. The difference between the optical and near-IR temperatures is largest between 3500 and 4200 K, where the fluxes below $0.75 \mu\text{m}$ transit rapidly from being almost nil to being large. Eye inspection of the fits shows that the best fit models sometimes deviate wildly from the “data” in the range *not* included in the fitting procedure, while over the range really used fits are dangerously good. When optical and near-IR spectra are used jointly, compensations occur and the correct Teff is recovered (to within ± 100 K) below 4200 K. Positive offsets of up to 400 K however persist above this temperature for all gravities.

The output $\log(g)$ equals the input $\log(g)$ below about 4300 K when using near-IR data, and is higher by one $\log(g)$ -sampling step at higher temperatures. When using optical data, the behaviour depends more strongly on the actual value of the input $\log(g)$. For high gravities, $\delta \log(g)$ is positive (one sampling step) at $T_{\text{eff}} > 3600$ K. For low

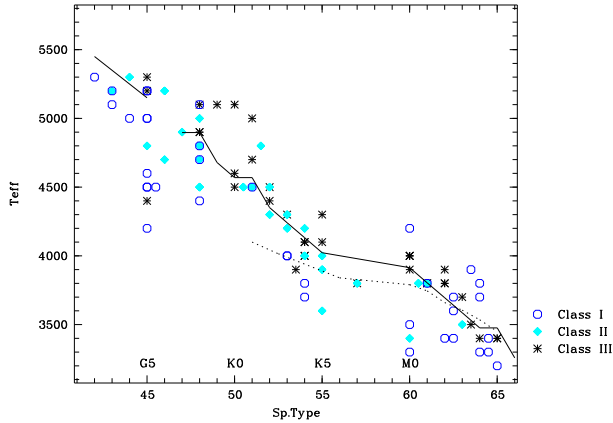


Fig. 21. Effective temperatures derived from fits to near-IR spectra ($\lambda > 0.97 \mu\text{m}$), compared with trends in the literature. RSG-specific abundances are used for class I stars, solar abundances for classes II and III. Solid lines: temperature scale for giants, from van Belle et al. (1999) for $T_{\text{eff}} < 5000 \text{ K}$ and from Schmidt-Kaler (1982) for $T_{\text{eff}} > 5000 \text{ K}$. Dotted line: temperature scale for supergiant stars from Levesque et al. (2005). Default spectral types from the SIMBAD database (operated at CDS, Strasbourg, France) are used for this figure.

gravities, $\delta \log(g)$ is nil at the lowest and highest temperatures, but peaks with a value $+2$ around 4200 K .

We note that corresponding plots can be produced for the “extinction”-correction A_V (which accounts for colour changes in the analysed wavelength ranges reasonably well). The qualitative aspects of the graphs for δA_V are similar to those of δT_{eff} , with a maximal amplitude of ± 0.6 magnitudes.

For comparison, we have performed a limited exploration of the effects of metallicity (with solar scaled abundance ratios) on the derived temperatures. Models at $\log(Z/Z_{\odot}) = -0.3$ were computed for $\log(g) = 1$ and -0.5 , and best fits to these were obtained using solar metallicity models. Plots similar to those in Fig. 20 were constructed. The effects of the change in Z on the derived T_{eff} is notably *smaller* than those just described for modified abundance ratios. When using optical wavelengths, the trend expected from the well known metallicity-temperature degeneracy is found (lower temperatures are required at lower metallicity to produce similar optical band depths). The offset varies between 100 K (low T_{eff}) and 200 K (high T_{eff}). At near-IR wavelengths, the correct temperatures are recovered unchanged except for a few deviations of $\pm 100 \text{ K}$. In both wavelength ranges, however, gravities higher than input are derived (by one gravity bin). For complementary discussions on metallicity effects, we refer to Kučinskas et al. (2006) and Levesque et al. (2006).

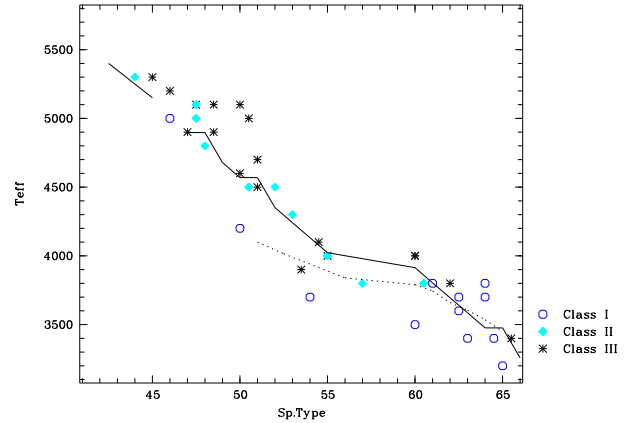


Fig. 22. Same as Fig. 21, but using only spectral types from Keenan & McNeil (1989) or Buscombe (1998). Using solar abundances moves the G6 supergiant in this figure down 200 K , the K0 supergiant up 100 K , and the M supergiants above 3600 K up by 100 to 200 K .

6.3. T_{eff} estimates for real stars

Figure 21 compares the effective temperatures derived in this paper from near-IR spectra with temperature scales from the literature. For giants, the plotted reference scale (below 5000 K) is based on angular diameter measurements (van Belle et al. 1999). The number of red supergiants with angular diameter measurements is small. For supergiants, we therefore show the scale recently obtained from fits of MARCS model atmosphere spectra to optical spectra by Levesque et al. (2005). The agreement is good, but the scatter is large.

As a sanity check, we may restrict our data sample to stars with *optical* spectra and discard near-IR wavelengths ($\lambda > 1 \mu\text{m}$) in the fitting procedure. This provides temperatures that are *a priori* more directly related to spectral types. In addition, we keep only stars with MK spectral types from Keenan & McNeil (1989) or Buscombe (1998), and with small variability (according to the Simbad database information). *Using solar abundance models* for direct comparison with the results of Levesque et al. (2005), we find that 8 of the 9 stars in the subsample have estimated temperatures within less than 50 K of the reference relations. Most of the stars in the subsample are supergiants and all are of type K5 or later. Thus, in this range of parameters, there is no indication of a systematic difference between the temperatures derived from optical spectra using the new PHOENIX models or the MARCS models of Levesque et al. (2005).

To illustrate what fraction of the scatter in Fig. 21 may be due to spectral classification errors, Fig. 22 reproduces the graph using only MK spectral types from Keenan & McNeil (1989) or Buscombe (1998), when available. A considerable scatter remains. Some of it is due to the real scatter in the properties of the stars (surface abundances, gravity, unknown variability). For supergiants in particu-

lar, and especially at low temperatures, the scatter also reflects the large intrinsic uncertainties associated with the relatively poor quality of the model fits. We expect the spread to shrink once models with a wider range of parameters (surface abundances, micro-turbulent velocities) will have been computed.

We have also examined the diagrams of estimated T_{eff} vs. spectral type obtained when any available optical data is included in the fitting procedure. They are similar to those described above. Individual stars are moved by up to 200 K, but no systematic trend can be clearly identified (because the stars that move most are also those for which the fits are poorest). Despite the added difficulty of fitting a broader wavelength range, the final dispersion is not significantly enhanced.

7. Conclusions

We have presented two grids of PHOENIX models for the spectra of luminous cool stars, one at solar metallicity, the other with RSG-specific surface abundances. We have described the properties of these models and compared them with observations, with a focus on the molecular features found in near-IR spectra at resolution $\lambda/\Delta\lambda \simeq 1000$. At these wavelengths, red giants and supergiants dominate the integrated light of stellar populations. Our main conclusions are the following.

- Models must be computed with a wavelength sampling step of about 0.1 \AA in order to reproduce the low resolution near-IR spectra adequately.
- The solar metallicity models provide a very good representation of empirical spectra of giants of class III and of a large fraction of the luminous giants of class II. As expected, RSG-specific abundances are found inadequate for the modelling of the bulk of the giant stars (they are rejected because they provide poorer fits and lead to a zone of avoidance in the derived T_{eff} -distribution). RSG-specific abundances are favoured for some class II giants, which may have suffered mixing in excess of standard first dredge-up.
- Red supergiant spectra of spectral types G and K, and of luminosity class Ib (sometimes also Iab) can be reproduced reasonably well. Serious disagreements remain in the case of very luminous (Ia and some Iab) and of very cool supergiants (type M). RSG-specific abundances tend to improve the fits to strong CN bands, although the global effect on the fit quality is not as spectacular as one might have hoped. However, changing the surface abundance ratios has a significant impact on the derived effective temperatures (the effect is larger than that found when moving from $0.5 Z_{\odot}$ to Z_{\odot}). Therefore, it will remain necessary to account for this effect of stellar evolution in future model grids.
- While it is easy (relatively) to produce good fits to the spectra of either the J, *or* the H, *or* the K band spectra of luminous cool stars, it remains more difficult to reproduce all their optical and near-IR molecular bands

simultaneously. As a result, estimated stellar parameters (T_{eff} , $\log(g)$, A_V) depend on the spectral range of the analysis. The effects of changes in the surface abundances on these parameters also depend on the wavelengths under study.

- The T_{eff} scales derived from the comparison of a collection of near-IR stellar spectra ($1 - 2.4 \mu\text{m}$) with models are generally consistent with previous scales, albeit with considerable scatter. For cool red supergiants, the current uncertainties on individual estimated T_{eff} values frequently exceed $\pm 100 \text{ K}$.

About 20% of the analysed red supergiant spectra have such strong CN bands that they call for models with high micro-turbulent velocities, and/or even more surface nitrogen than we have considered, and/or for gravities lower than $\log(g) = -1$. The coolest of these are variable, and variability may contribute to the building of an extended atmosphere with low effective gravities. Large micro-turbulent velocities have been derived for a number of red supergiants in the past, and our first calculations confirm that increasing this parameter will help reproducing the spectra of type Ia supergiants. In particular, a better agreement with observations is expected for the ratio between the first and second overtone CO band strengths. A grid of models is currently being calculated. Somewhat higher nitrogen abundances than we have explored are expected to exist in nature, for instance when stellar rotation increases internal mixing. Because low resolution near-IR spectra of red supergiants are relatively easy to acquire, their comparison with models at the specific abundances predicted by stellar tracks with rotation will provide interesting tests of stellar evolution theory. Considering stars with lower gravities is a more challenging modelling task, as they will develop strong winds. In addition, the winds may be loaded with dust. Since winds are a well known empirical property of many red supergiants, the development of models that include winds is a necessity of the future.

Acknowledgements. PHH was supported in part by the Pôle Scientifique de Modélisation Numérique at ENS-Lyon and by Université Louis Pasteur at Strasbourg Observatory. Some of the calculations presented here were performed at the Höchstleistungs Rechenzentrum Nord (HLRN), and at the National Energy Research Supercomputer Center (NERSC), supported by the U.S. DOE, and at the computer clusters of the Hamburger Sternwarte, supported by the DFG and the State of Hamburg. We thank all these institutions for a generous allocation of computer time. We thank C. Charbonnel for insightful discussions of aspects of this work. This research has made use of the SIMBAD database and the VIZIER service, operated at CDS, Strasbourg, France. It uses data (in preparation for publication) acquired using the NASA Infrared Telescope Facility, Hawaii, USA, and the 2.3m Telescope of the Australian National University, Siding Spring, Australia.

References

- Anders, E., Grevesse, N. 1989, *Geochim. Cosmochim. Acta* 53, 197

- Asplund, M., Grevesse, N., Sauval, A.J. 2006, in *Cosmic Abundances as Records of Stellar Evolution and Nucleosynthesis*, T.G. Barnes, III, & F.N. Bash (eds.), ASP Conf. Ser. 336, 25
- Baldwin, J.R., Frogel, J.A., Persson, S.E. 1973, *ApJ* 184, 427
- Becker, S.A., & Iben, I., Jr. 1979, *ApJ* 232, 831
- Beer, R., Hutchison, R.B., Norton, R.H., Lambert, D.L. 1972, *ApJ* 172, 89
- Bessell, M.S., Brett, J.M. 1988, *PASP* 100, 1134
- Bessell, M.S., Brett, J.M., Scholz, M., & Wood, P.R. 1989, *A&AS* 77, 1
- Bessell, M.S., Brett, J.M., Scholz, M., & Wood, P.R. 1991, *A&AS* 89, 335
- Boothroyd, A.I., & Sackmann, I.-J. 1999, *ApJ* 510, 232
- Bressan, A., Fagotto, F., Bertelli, G., Chiosi, C. 1993, *A&AS* 100, 647
- Buscombe, 1998, Illinois catalogue of MK spectral classifications (version 13), Northwestern Univ. Evanston, Illinois.
- Cardelli, J.A., Clayton, G.C. & Mathis, J.S. 1989, *ApJ* 345, 245
- Charbonnel, C. 1994, *A&A* 282, 811
- Charbonnel, C. & do Nascimento, J.D., Jr. 1998, *A&A* 336, 915
- Charbonnel C., Meynet, G., Maeder, A., Schaerer, D. 1996, *A&AS* 115, 339
- Decin, L., Shkedy, Z., Molenberghs, G., Aerts, M., Aerts, C. 2004, *A&A* 421, 281
- Frogel, J.A., Persson, S.E., Aaronson, M., Matthews, K. 1978, *ApJ* 220, 75
- Girardi, L., Bressan, A., Bertelli, G., Chiosi, C. 2000, *A&AS* 141, 371
- Goorvitch, D., & Chackerian, C. 1994, *ApJS* 91, 483
- Goorvitch, D., & Chackerian, C. 1994, *ApJS* 92, 311
- Grevesse, N. 1991, in *Evolution of Stars: the Photospheric Abundance Connection*, G. Michaud & A.V. Tutukov (Eds.), Kluwer (Dordrecht), IAU Symp. 145, 63
- Grevesse, N., & Noels, A. 1993, in *Origin and Evolution of the Elements*, N. Prantos, E. Vangioni-Flam & M. Cassé (Eds.), Cambridge Univ. Press, 14
- Iben, I., Jr. 1964, *ApJ* 140, 1631
- Iben, I., 1966, *ApJ* 143, 516
- Keenan, P.C., McNeil, R.C. 1989, *ApJSS* 71, 245
- Kučinskas, A., Hauschildt, P.H., Ludwig, H.-G., Brott, I., Vansevičius, V., Lindegren, L., Tanabé, T., Allard, F. 2005, *A&A*, 442, 281
- Kučinskas, A., Hauschildt, P.H., Brott, I., Vansevičius, V., Lindegren, L., Tanabé, T., Allard, F. 2006, *A&A* 452, 1021
- Lançon, A., Wood, P.R. 2000, *A&AS* 146, 217
- Lançon, A., Smith, L.J., Gallagher, J.S. et al. 2003, in *Extragalactic Globular Clusters and their Host Galaxies* (IAU JD 6, ed. T. Bridges), *Highlights of Astronomy* 13, ed. O. Engvold, in press
- Lançon, A., Wood, P.R., Ladjal, D., Mouhcine, M., Gallagher, J.S., Smith, L.J., Vacca, B., Förster Schreiber, N., de Grijs, R., O'Connell, R. 2007, in preparation
- Levesque, E.M., Massey, P., Olsen, K.A.G., Plez, B., Josselin, E., Maeder, A., Meynet, G. 2005, *ApJ* 628, 973
- Levesque, E.M., Massey, P., Olsen, K.A.G., Plez, B., Meynet, G., Maeder, A. 2006, *ApJ* 645, 1102
- Loidl, R., Lançon, A., Jorgensen, U.G. 2001, *A&A* 371, 1065
- Maeder, A. 1981, *A&A* 101, 385
- Maeder, A., & Meynet, G. 2001, *A&A* 373, 555
- Martins, L.P., González Delgado, R.M., Leitherer, C., Cerviño, M., Hauschildt, P.H. 2005, *MNRAS* 358, 49
- McGregor, P.J. 1987, *ApJ* 312, 195
- McWilliam, A., & Lambert, D.L. 1984, *PASP* 96, 882
- Meynet, G., & Maeder, A. 2000, *A&A* 361, 101
- Meynet, G., & Maeder, A. 2003, *A&A* 404, 975
- Meynet, G., Maeder, A., Schaller, G., Schaerer, D., Charbonnel, C. 1994, *A&AS* 103, 97
- Origlia, L., Moorwood, A.F.M., Oliva, E. 1993, *A&A* 280, 536
- Origlia, L., Ferraro, F.R., Fusi Pecci, F., Oliva, E. 1997, *A&A* 321, 859
- Schaller, G., Schaerer, D., Meynet, G., Maeder, A. 1992, *A&AS* 96, 269
- Schmidt-Kaler 1982, in *Astrophysical Data: Planets & Stars* (1992), Lang N. (Ed.), Springer (New York)
- Schwenke, D.W. 1998, in *Chemistry & Physics of Molecules and Grains in Space*. Faraday Discussions No. 109 (Royal Soc. of Chemistry, London) p.321.
- Smith, V.V., & Lambert, D.L. 1985, *ApJ* 294, 326
- Trundle, C., & Lennon, D.J. 2005, *A&A* 434, 677
- Tsuji, T. 1976, *PASJ* 28, 543
- van Belle, G.T., Lane, B.F., Thompson, R.R. et al. 1999, *AJ* 117, 521
- Vanhollebeke, E., Blommaert, J.A.D.L., Schultheis, M., Aringer, B., Lançon, A. 2006, *A&A* 455, 645
- White, N.M., Wing, R.F. 1978, *ApJ* 222, 209
- Wing, R.F., & Spinrad, H. 1970, *ApJ* 159, 973